ISSN: 2472-3703 DOI: 10.6911/WSRJ.202611_12(11).0009

Pressure Control Method for a Zone-Controlled Crown Roll Hydraulic Loading System Based on IFE-WOA-Optimized Variable-Universe Fuzzy PID Control

Lihui Meng[1, 2, *]

[1]School of Construction Machinery, Shandong Jiaotong University, Jinan, China.

[2]Shandong Provincial Engineering Research Center for Transportation Construction Equipment Technology and Intelligent Construction, Shandong Jiaotong University, Jinan, China.

[*]Corresponding author's e-mail addresses: 15550028176@163.com

Abstract

To improve loading-pressure regulation of zone-controlled crown rolls under multi-level pressure switching, valve-controlled nonlinearity, and local coupling-related disturbances, this study develops an IFE-WOA-optimized variable-universe fuzzy PID control method. An AMESim hydraulic model is coupled with MATLAB/Simulink for controller design and evaluation. A constraint-derived rational input mapping is introduced to preserve small-error sensitivity while compressing large normalized inputs. The initial PID gains and fuzzy input/output scaling factors are jointly optimized using a multi-condition objective that covering nominal tracking and disturbance rejection. Intuitionistic fuzzy entropy is used to characterize the population state and regulate an entropy-driven escape mechanism in IFE-WOA, while bounded gain projection, actuator saturation, and tracking anti-windup ensure physically realizable control. Co-simulation results show that, relative to conventional PID control, the proposed method reduces normalized ITAE, maximum relative overshoot, and average relative steady-state error by 64.33%, 51.30%, and 73.94%, respectively. In the 15 s negative-disturbance window, peak absolute error and IAE are reduced by 57.89% and 66.54%. Benchmark tests show lower mean final objective values on five of six functions, with statistically significant improvements on Rosenbrock and Rastrigin after Holm correction. The results demonstrate improved tracking, pressure holding, and disturbance recovery under the investigated operating conditions.

Keywords

Variable-universe fuzzy PID control; intuitionistic fuzzy entropy; whale optimization algorithm; zone-controlled crown roll.

1. INTRODUCTION

The operating quality of the press and calender sections in high-speed wide paper machines strongly depends on the uniformity of nip line pressure distribution across the machine width. Under heavy-load and wide-width operating conditions, roll bending deflection can easily lead to nonuniform nip pressure distribution, thereby affecting key paper quality indices such as thickness, smoothness, and moisture content. A zone-controlled crown roll applies adjustable support forces to the roll shell through multiple hydraulic loading units arranged along the axial direction, enabling compensation for line-pressure deviations at different cross-machine positions. It therefore serves as an important actuator for cross-directional quality control in

ISSN: 2472-3703 DOI: 10.6911/WSRJ.202611_12(11).0009

paper machines. Cross-directional control systems exhibit evident spatially distributed characteristics, and their control performance is generally affected by multi-actuator coupling, process uncertainty, and actuator constraints [1]. For cross-directional systems with approximate symmetries, structural approximations and modeling errors may further influence the closed-loop stability, control performance, and robustness of large-scale high-speed process control systems [2]. These considerations indicate that the ability of each loading zone to provide stable, adjustable, and consistent support force is a key factor determining the effectiveness of cross-directional line-pressure compensation.In a zone-controlled crown roll, the hydraulic loading system generally consists of a hydraulic power unit, main oil supply pipeline, proportional pressure-reducing valves, hydraulic cylinders, pressure sensors, pressure-holding elements, and return-oil branches. After pressurized oil enters each loading zone through the main oil supply pipeline, the pressure of each zone is regulated by an electro-hydraulic proportional valve and then converted by the hydraulic cylinder into a radial support force acting on the roll shell. This pressure regulation and force conversion process makes the pressure control performance of a single zone directly related to local loading-force stability and cross-directional line-pressure compensation accuracy. Since the electro-hydraulic loading process exhibits pronounced nonlinear characteristics, parameter uncertainty, external disturbances, friction, output constraints, and complex load effects may amplify pressure tracking errors and weaken dynamic response performance [3-6]. In electro-hydraulic servo and axis systems, sensor faults, unknown time-varying parameters, and matched or mismatched disturbances can also degrade tracking accuracy, system reliability, and closed-loop stability [7, 8]. For multi-actuator parallel hydraulic systems, branch flow distribution, pressure matching, and cross-coupling further affect the consistency of pressure responses among different zones [9]. If flow nonlinearity in valve-controlled or independent-metering hydraulic systems is not accurately modeled and effectively compensated, the pressure or motion control accuracy of the system will also deteriorate significantly [10].

High-precision pressure control of a zone hydraulic loading system depends not only on an accurate description of the dynamic characteristics of the hydraulic plant, but also on the adaptability of controller parameters to changing operating conditions. Studies on load-sensitive hydraulic systems have shown that when the pressure/flow output does not match the load demand, system stability, control accuracy, and energy utilization efficiency are affected [11]. Research on variable pumps and pump-controlled electro-hydraulic actuators further indicates that nonlinear dynamics, parameter uncertainty, disturbance rejection, and actuator constraints are important factors affecting hydraulic pressure or motion control performance [12-14]. In recent years, artificial-intelligence-assisted and data-driven control methods have been applied to hydraulic systems to improve the control accuracy and robustness of nonlinear actuators under uncertainty and disturbances [15, 16]. Recent optimal predictive control studies further show that combining online disturbance forecasting with multi-objective PID-type parameter optimization can improve transient regulation, damping performance, and operating economy under time-varying operating conditions [17]. Fuzzy PID control has relatively low dependence on an exact model and can update control gains online according to the pressure error and its variation trend. It is therefore suitable for hydraulic systems with valve-orifice flow nonlinearity, load disturbances, and parameter uncertainty. The application of fuzzy logic to uncertainty handling in hydraulic and pneumatic systems also provides a methodological basis for applying fuzzy PID to pressure regulation [18]. Meanwhile, observer-based electro-hydraulic control studies show that estimating unmeasured states and lumped disturbances helps improve control stability under uncertainty [19]. These approaches motivate the consideration of disturbance-related performance evaluation in hydraulic control systems. On the basis of fuzzy PID control, the variable-universe mechanism dynamically adjusts the fuzzy universe of discourse, enabling the controller to maintain a wider regulation

ISSN: 2472-3703 DOI: 10.6911/WSRJ.202611_12(11).0009

range during large-error stages and improve inference resolution in small-error regions. Nevertheless, variable-universe fuzzy PID performance still depends on the coordinated selection of initial PID parameters and input/output scaling factors. For the zone-controlled crown roll hydraulic loading system, pressure-platform switching and varying disturbance characteristics make empirical tuning unable to simultaneously satisfy full-process tracking and local disturbance suppression requirements.

The variable-universe fuzzy PID controller involves multiple coupled parameters, including initial PID gains, input scaling factors, and output scaling factors. Therefore, manual empirical tuning alone makes it difficult to obtain a parameter combination that simultaneously balances tracking accuracy, steady-state pressure holding, and disturbance suppression over a large search space. This limitation is consistent with recent PID tuning studies in automatic generation control, where multi-objective evolutionary optimization has been used to balance ITAE/ITSE-type error indices, deviation-rate criteria, convergence speed, overshoot suppression, and stability rather than relying on a single empirical tuning objective [20]. Swarm intelligence algorithms have global search capability and are suitable for such multi-parameter coordinated optimization problems. A recent survey on Q-learning-assisted meta-heuristic optimization further indicates that adaptive parameter control, operator selection, and exploration-exploitation balancing are key mechanisms for improving optimizer robustness in engineering applications [21]. The Whale Optimization Algorithm (WOA) is a swarm intelligence optimization algorithm inspired by the bubble-net hunting behavior of humpback whales. It has the advantages of a simple structure, few parameters, and ease of implementation, and has been widely used in engineering optimization problems. To overcome premature convergence, insufficient population diversity, and weak local search in standard WOA, recent studies have introduced multi-strategy mechanisms, multi-population evolution, and enhanced updating strategies to improve its exploration–exploitation balance and engineering optimization performance [22-26]. In addition, multi-objective PID optimization studies have incorporated WOA-derived spiral search, quasi-opposition learning, and Q-learning to enhance population diversity, improve escape from local optima, and strengthen robustness against load-disturbance uncertainty [27]. From the overall research progress, WOA and its improved variants have been widely applied to engineering optimization, but their performance is still affected by population diversity, parameter update mechanisms, and the specific optimization object [28]. In hydraulic controller parameter tuning, the Intuitionistic Fuzzy Entropy-Improved Whale Optimization Algorithm (IFE-WOA) has been combined with fuzzy PID control for speed regulation of a complex hydraulic transmission system, indicating the feasibility of entropy-assisted swarm intelligence optimization for hydraulic controller tuning [29]. Existing studies mainly focus on general hydraulic transmission systems, benchmark optimization problems, or single actuators, whereas multi-pressure-platform tracking, adjacent-zone coupling disturbances, and local disturbance-window error suppression in zone-controlled crown roll hydraulic loading systems remain insufficiently investigated. Accordingly, the remaining issue is not PID-gain optimization alone, but the coordinated design of offline multi-parameter optimization and online gain adaptation for zone-controlled crown roll pressure regulation under multi-level loading and local disturbance conditions.

Hence, this study focuses on the coordinated design of offline parameter optimization and online variable-universe fuzzy gain adjustment for pressure regulation of a zone-controlled crown roll hydraulic loading system. An AMESim hydraulic model is established and coupled with MATLAB/Simulink for controller design and evaluation. A constraint-derived rational input mapping is introduced into the variable-universe fuzzy PID controller to preserve small-error sensitivity while satisfying monotonicity, non-expansiveness, and boundedness, thereby smoothly compressing large normalized inputs during multi-level pressure switching. The offline tuning problem is formulated as a joint optimization of the initial PID gains and the fuzzy

ISSN: 2472-3703 DOI: 10.6911/WSRJ.202611_12(11).0009

input/output scaling factors under a multi-condition objective incorporating both nominal tracking and local disturbance-rejection requirements. Intuitionistic fuzzy entropy is further used as population-state information to regulate the escape operation of IFE-WOA, while the optimized parameters provide the baseline for subsequent online fuzzy gain adjustment. The proposed framework is evaluated from both algorithmic and controller-implementation perspectives through weighting-coefficient sensitivity analysis, mechanism ablation, repeated-run statistical benchmark tests, disturbance-window evaluation, and verification of bounded online gains, actuator saturation, and tracking anti-windup behavior.

2. MODELING AND PARAMETER SETTING OF THE ZONE-CONTROLLED CROWN ROLL HYDRAULIC LOADING SYSTEM

To analyze the cross-directional line-pressure regulation characteristics of the hydraulic loading system, an AMESim hydraulic simulation model is constructed, as shown in Figure 1. The model includes the main oil supply circuit, zone supply manifold, representative single-zone loading branch, and pressure closed-loop control unit. The main hydraulic circuit supplies oil to zones G1-G4 through the main pressure supply pipeline, and each zone is connected to multiple sub-zone loading branches to realize segmented pressure regulation along the roll axis. In Figure 1, Z01 is selected as a typical single-zone loading branch to describe the pressure feedback regulation process of each small-zone loading unit. The electro-hydraulic proportional pressure-reducing valve adjusts its opening according to

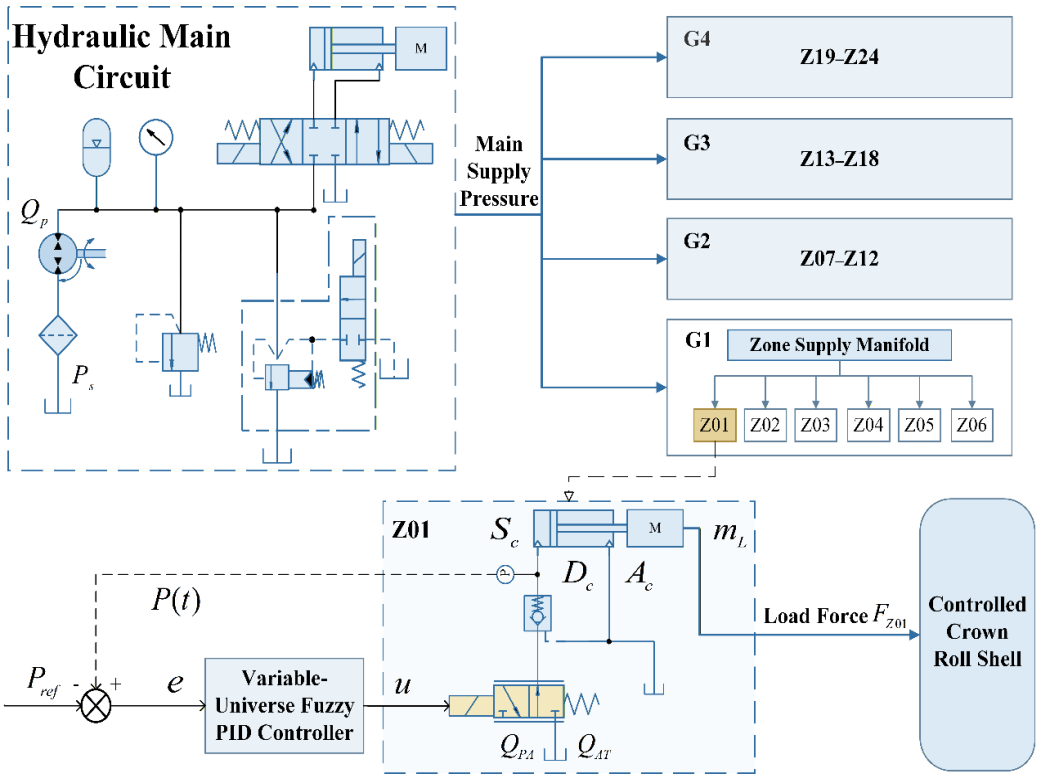


Figure 1. Structure of the zone-controlled crown roll hydraulic loading system and block diagram of single-section pressure closed-loop control

the controller output current, thereby regulating the hydraulic cylinder chamber pressure. The hydraulic cylinder converts hydraulic pressure into a local supporting force acting on the crown

ISSN: 2472-3703 DOI: 10.6911/WSRJ.202611_12(11).0009

roll shell, while the pressure sensor feeds the actual pressure back to the controller to form a closed-loop pressure control system for single-zone loading.

Table 1 lists the representative nominal parameters used to establish a consistent AMESim plant for controller design and comparative evaluation. In practical operation, fluid properties, leakage, valve characteristics, and actuator dynamics may vary with operating conditions. The present study therefore treats these values as nominal settings and evaluates controller behavior under multi-level loading, plant-side disturbances, and implementation constraints.

Table 1. Main symbols and simulation parameters of the main oil supply circuit and representative sub-zone loading branch

Parameter	Symbol	Unit	Value
Pump supply pressure	P_s	bar	120
Rated pump flow rate	Q_p	$L \cdot min^{-1}$	42
Bulk modulus	β_e	bar	1.7×10^4
Hydraulic oil density	ρ	$kg \cdot m^{-3}$	850
Dynamic viscosity	μ	cP	39
Characteristic flow of P-A channel of proportional pressure-reducing valve	Q_{PA}	$L \cdot min^{-1}$	10
Characteristic flow of A-T channel of proportional pressure-reducing valve	Q_{AT}	$L \cdot min^{-1}$	2
Control input range of proportional pressure-reducing valve	u	mA	0–40
Piston diameter	D_c	mm	50
Effective piston area	A_c	m^2	1.96×10^{-3}
Hydraulic cylinder stroke	S_c	mm	10
Equivalent load mass	m_L	kg	30

As shown in Figure 2, the main supply pressure and pump flow rate exhibit coordinated variations during the simulated operation, indicating that the hydraulic source can provide stable pressure and flow support for the subsequent zone-control loading process.

ISSN: 2472-3703 DOI: 10.6911/WSRJ.202611_12(11).0009

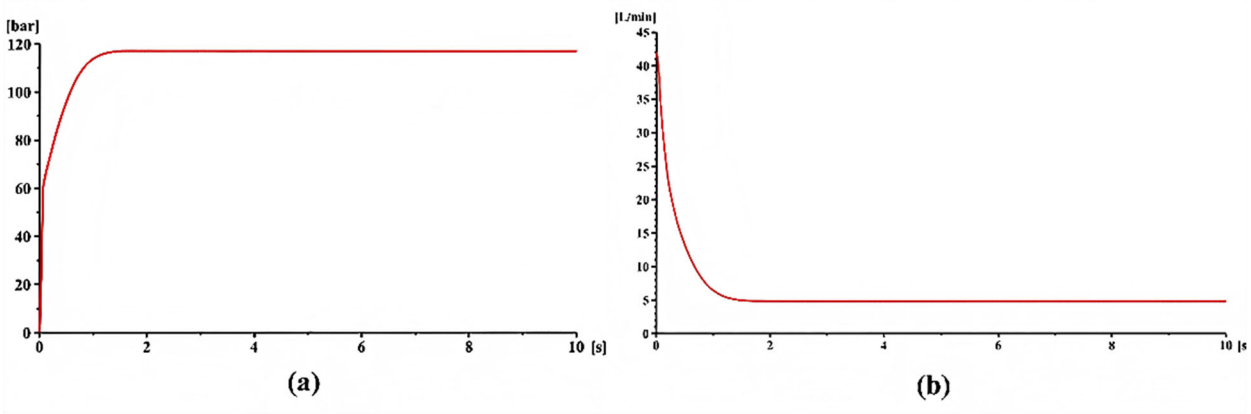


Figure 2. Dynamic responses of the main hydraulic supply circuit obtained from the AMESim model: (a) Main supply pressure and (b) Main pump flow rate

Figure 3 shows coordinated pressure, valve, flow-rate, and cylinder-displacement transients in the representative loading branch, supporting the use of the developed AMESim model for subsequent controller evaluation.

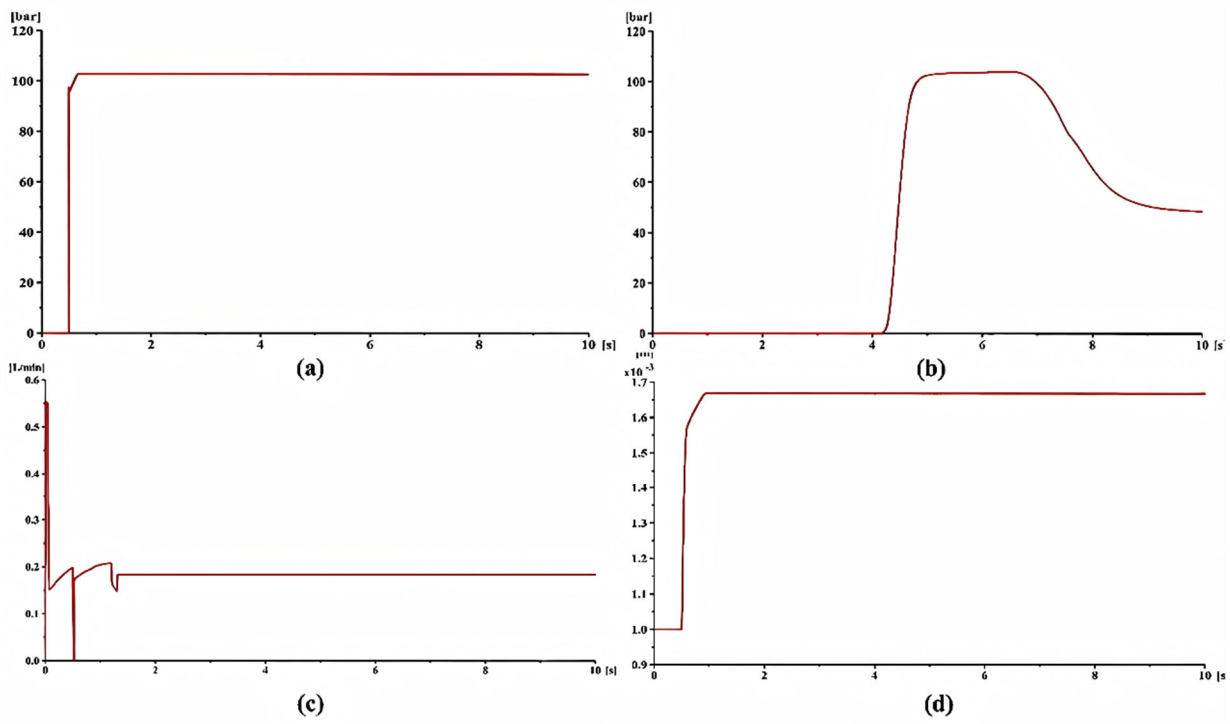


Figure 3. Dynamic responses of the zone-control hydraulic loading branch in the AMESim model: (a) pressure step response of a single zone, (b) directional-valve pressure response, (c) flow-rate response during the pressure step process, and (d) hydraulic-cylinder displacement response of the single zone

3. IFE-WOA-OPTIMIZED VARIABLE-UNIVERSE FUZZY PID PRESSURE CONTROL METHOD

3.1. Overall Control Architecture

As shown in Figure 4, the proposed method comprises an online pressure-control layer and an offline parameter-optimization layer. In the online layer, the pressure error and its rate of

ISSN: 2472-3703 DOI: 10.6911/WSRJ.202611_12(11).0009

change are normalized and processed by the constraint-derived rational mapping before fuzzy inference. The fuzzy outputs adjust the PID gains online, after which bounded gain projection, actuator saturation, and tracking anti-windup ensure physically realizable control. In the offline layer, the initial PID gains and input/output scaling factors are jointly optimized under nominal and disturbed operating conditions using the multi-condition objective. IFE-WOA evaluates the population state through intuitionistic fuzzy entropy and activates an entropy-driven escape mechanism to reduce premature-convergence risk. The optimized parameter vector is then transferred to the online controller as the baseline for subsequent gain adjustment. Thus, IFE-WOA is not used solely to determine a fixed PID-gain triplet; it coordinates the baseline gains and fuzzy scaling parameters that shape the online adaptation process.

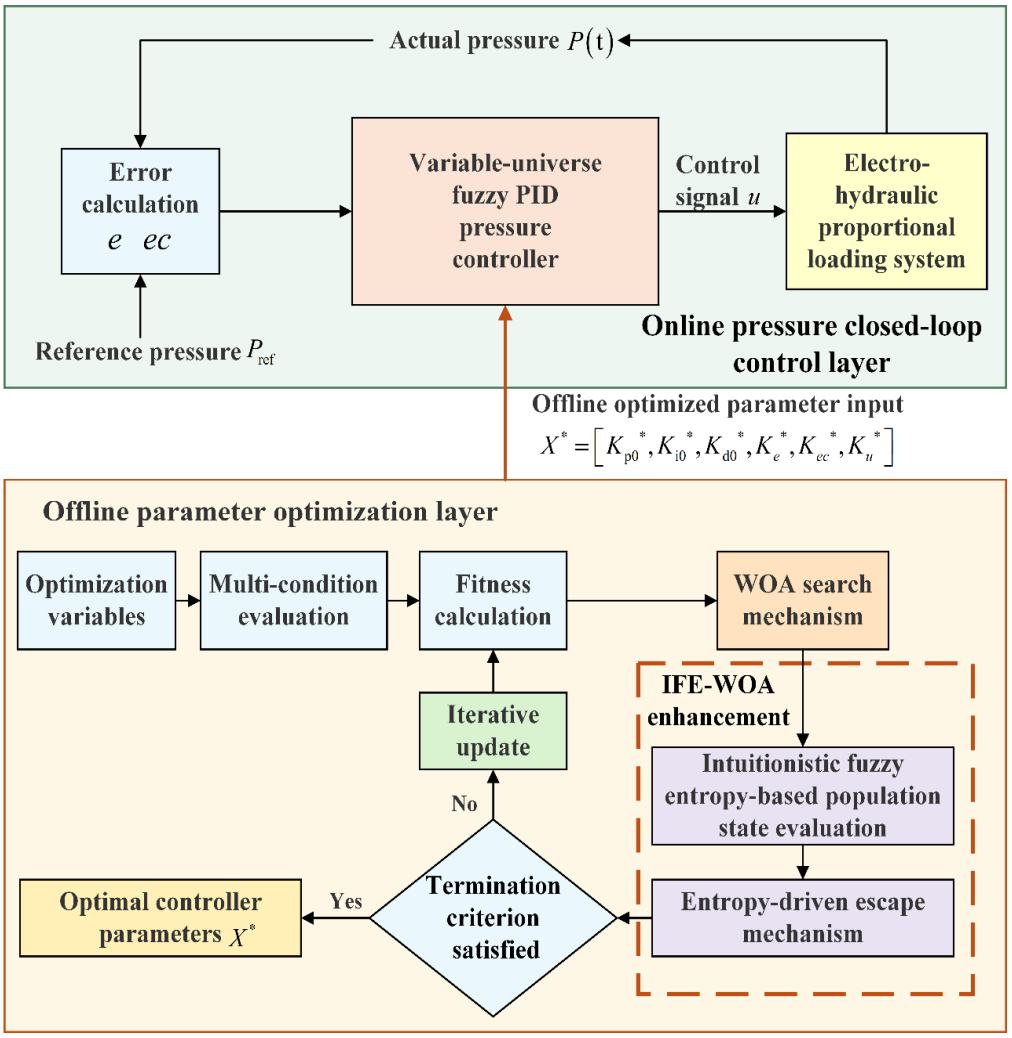


Figure 4. Overall framework of the IFE-WOA-optimized variable-universe fuzzy PID pressure control method

3.2. Design of the Variable-Universe Fuzzy PID Controller

3.2.1 Overall Structure of the Variable-Universe Fuzzy PID Controller

Based on the established hydraulic loading system model and the overall control framework, zone loading pressure regulation exhibits pronounced nonlinearity, time-varying characteristics, and disturbance sensitivity. Its dynamic response is jointly affected by the flow characteristics of the proportional pressure-reducing valve, hydraulic oil compressibility, actuator inertia, and coupling between adjacent zones. A fixed-parameter PID controller is difficult to satisfy the requirements of rapid pressure build-up, steady-state pressure holding,

ISSN: 2472-3703 DOI: 10.6911/WSRJ.202611_12(11).0009

and disturbance suppression under different pressure platforms and disturbance conditions. Nonlinear dynamics, uncertainties, constraints, and disturbances represent major challenges in electro-hydraulic control systems. Existing studies have addressed these issues through approaches such as ESO-based adaptive control, neural-network-assisted sliding-mode control, and finite-time adaptive backstepping control [30-32]. These methods provide effective solutions for nonlinear disturbance rejection; however, their implementation usually requires additional observers, adaptive laws, or system-specific design procedures. In this study, a variable-universe fuzzy PID controller is adopted because it provides a relatively simple structure while enabling online gain adjustment and compatibility with the existing hydraulic control architecture.

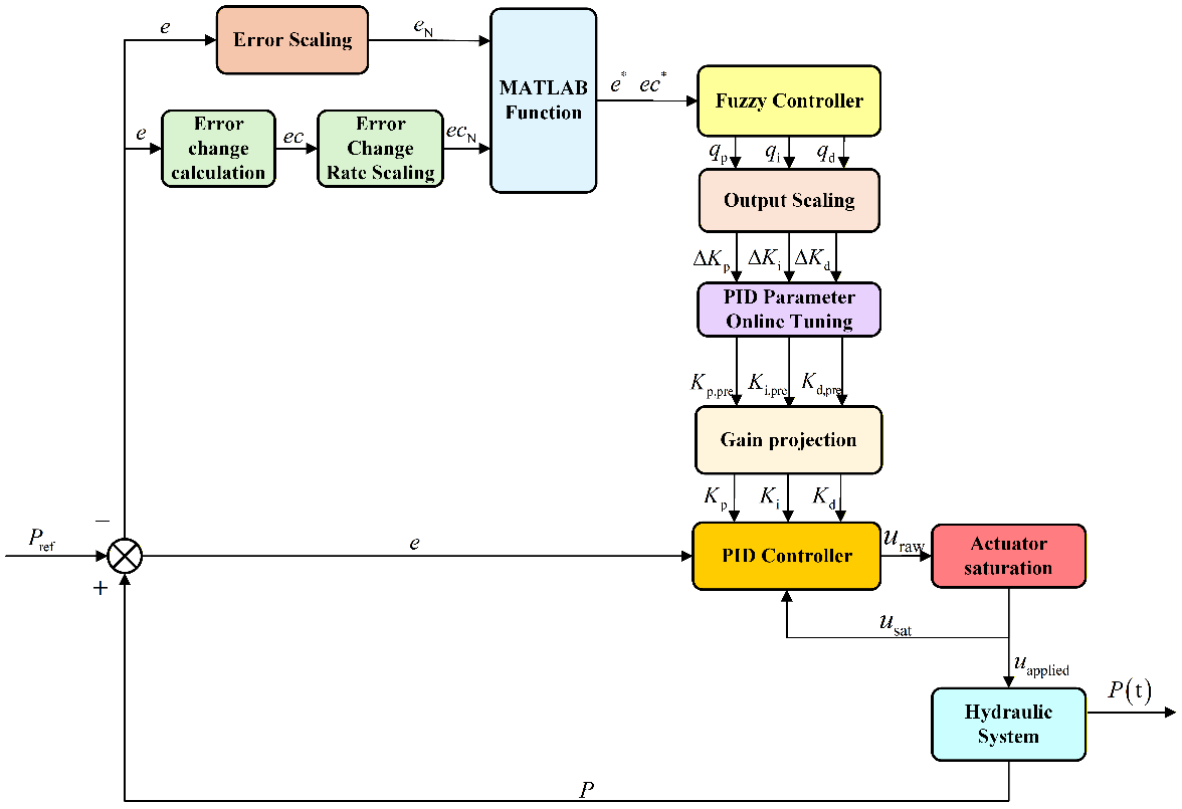


Figure 5. Structure of the variable-universe fuzzy PID controller for zone loading pressure regulation

The controller structure is shown in Figure 5. The controller takes the pressure error $e = P(t) - P_{\text{ref}}$ and the error rate $ec = \dfrac{\mathrm{d}e}{\mathrm{d}t}$ as input variables to characterize the instantaneous pressure tracking state. After fuzzification and rule inference, the fuzzy module produces the normalized outputs q_{p}, q_{i}, and q_{d}, each of which lies within the normalized output universe $[-1,1]$. These dimensionless outputs are converted through channel-specific output scaling into the gain correction increments ΔK_{p}, ΔK_{i}, and ΔK_{d}, respectively. The resulting correction increments are then used to update the proportional, integral, and derivative gains online. After bounded gain projection, the PID controller generates the actuator command for closed-loop regulation of the zone loading pressure.

ISSN: 2472-3703 DOI: 10.6911/WSRJ.202611_12(11).0009

The normalized fuzzy outputs are converted into numerical values using the centroid defuzzification method and are subsequently transformed into the corresponding gain correction increments through output scaling:

$$q_j(t)=\frac{\sum_{\ell=1}^{n}\xi_\ell\mu_j(\xi_\ell,t)}{\sum_{\ell=1}^{n}\mu_j(\xi_\ell,t)},\qquad \Delta K_j(t)=S_j q_j(t),\qquad j\in\{p,i,d\} \tag{1}$$

Here, q_{j} denotes the normalized output of the j-th fuzzy inference channel; $\xi_\ell\in[-1,1]$ is the ℓ-th discrete sampling point in the normalized output universe; $\mu_j(\xi_\ell,t)$ is the corresponding aggregated output membership degree; n is the number of discrete sampling points; and S_j is the effective output scaling coefficient of the corresponding gain-correction channel. Accordingly, q_{j} is dimensionless, whereas ΔK_j has the same dimension as the associated PID gain.

After the gain correction increments are obtained, the preliminary PID gains before bounded projection are formed as follows:

$$\begin{cases}K_{\mathrm{p,pre}}(t)=K_{\mathrm{p0}}+\Delta K_{\mathrm{p}}(t)\\ K_{\mathrm{i,pre}}(t)=K_{\mathrm{i0}}+\Delta K_{\mathrm{i}}(t)\\ K_{\mathrm{d,pre}}(t)=K_{\mathrm{d0}}+\Delta K_{\mathrm{d}}(t)\end{cases} \tag{2}$$

Here, $K_{\mathrm{p,pre}}$, $K_{\mathrm{i,pre}}$ and $K_{\mathrm{d,pre}}$ denote the preliminary gains generated by fuzzy online correction. The gains actually supplied to the PID controller are obtained after bounded projection, as described in Section 3.2.4.

3.2.2 Fuzzy Rules and Membership Functions

Each fuzzy input and output variable is described using seven distinct linguistic terms: NB, NM, NS, ZO, PS, PM, and PB. The corresponding linguistic variable partition is shown in Table 2.

Table 2. Linguistic levels of fuzzy inference variables

Symbol	Fuzzy Linguistic
NB	Negative Big
NM	Negative Medium
NS	Negative Small
ZO	Zero
PS	Positive Small
PM	Positive Medium
PB	Positive Big

The rule base is designed according to the sign and magnitude of the pressure error and its variation trend. When the system is in an under-pressure or over-pressure state with a large error magnitude, the proportional action is increased to accelerate pressure error correction. When the error changes rapidly, the derivative correction is enhanced to suppress pressure overshoot and error expansion. When the pressure error is small, the integral correction is

ISSN: 2472-3703 DOI: 10.6911/WSRJ.202611_12(11).0009

appropriately strengthened to reduce residual steady-state error. Based on these principles, the fuzzy control rules for ΔK_p, ΔK_i, and ΔK_d are established, as shown in Figure 6.

ΔK_p	NB	NM	NS	ZO	PS	PM	PB
NB	PB	PB	PB	PM	PS	PS	PS
NM	PM	PM	PM	PS	ZO	ZO	ZO
NS	PS	PS	PS	ZO	NS	NS	NS
ZO	NS	NS	NS	NS	NS	NS	NS
PS	NS	NS	NS	ZO	PS	PS	PS
PM	ZO	ZO	ZO	PS	PM	PM	PM
PB	PS	PS	PS	PM	PB	PB	PB

ΔK_i	NB	NM	NS	ZO	PS	PM	PB
NB	NB	NB	NB	NM	NM	NM	NM
NM	NM	NM	NM	NS	NS	NS	NS
NS	NS	NS	NS	ZO	ZO	ZO	ZO
ZO	PS	PS	PS	PS	PS	PS	PS
PS	ZO	ZO	ZO	ZO	NS	NS	NS
PM	NS	NS	NS	NS	NM	NM	NM
PB	NM	NM	NM	NM	NB	NB	NB

ΔK_d	NB	NM	NS	ZO	PS	PM	PB
NB	PB	PM	PS	NS	NS	ZO	PS
NM	PB	PM	PS	NS	NS	ZO	PS
NS	PB	PM	PS	NS	NS	ZO	PS
ZO	PM	PS	ZO	NS	ZO	PS	PM
PS	PS	ZO	NS	NS	PS	PM	PB
PM	PS	ZO	NS	NS	PS	PM	PB
PB	PS	ZO	NS	NS	PS	PM	PB

Figure 6. Fuzzy rules for ΔK_p, ΔK_i, and ΔK_d

The basic universes of the input variables e and ec are determined according to the error variation ranges during pressure switching and disturbance recovery. The universe of e is set to $[-60,60]$, which covers the main pressure error range during pressure rise, pressure drop, and disturbance recovery. The universe of ec is set to $[-12000,12000]$, which characterizes rapid error variation under pressure step changes and disturbance conditions. Z-shaped and S-shaped membership functions are used in the boundary regions so that large positive and negative errors can be stably assigned to PB or NB, preventing the inputs from exceeding the effective fuzzy inference range. Triangular membership functions are used in the middle region to improve inference sensitivity near medium and small errors. This setting ensures the effective fuzzy inference range of the input variables and provides a basis for the subsequent nonlinear input-side scaling mapping, thereby improving error resolution near steady-state conditions. The membership functions of the input variables e and ec are shown in Figures 7 and 8.

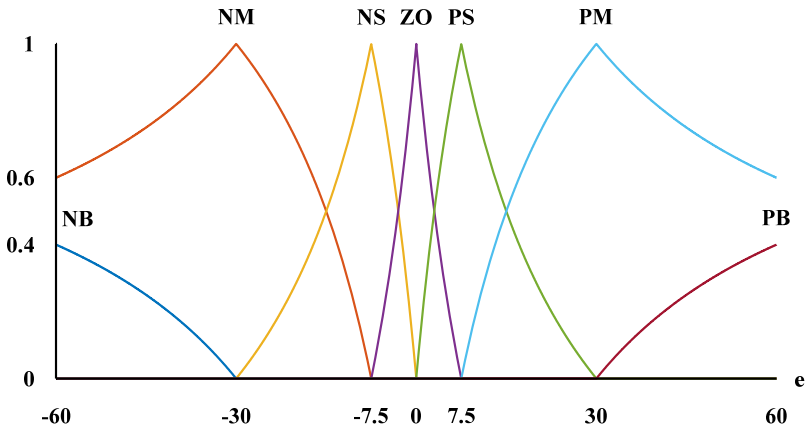


Figure 7. Membership function curves of e

ISSN: 2472-3703 DOI: 10.6911/WSRJ.202611_12(11).0009

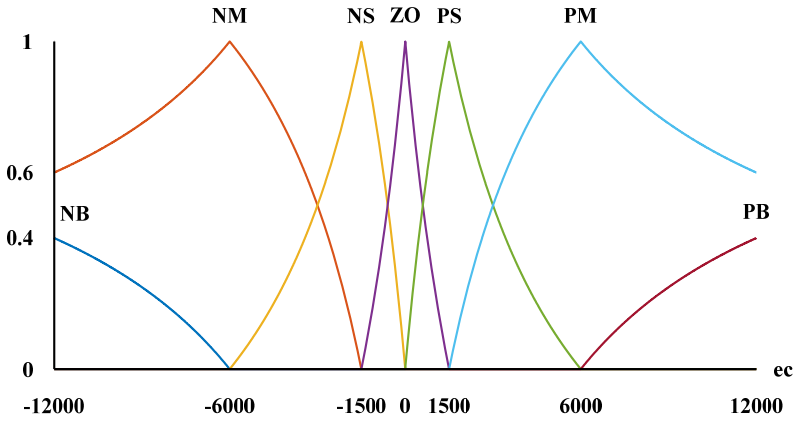


Figure 8. Membership function curves of ec

The normalized fuzzy output variables q_p, q_i, and q_d are defined over the common dimensionless universe $[-1,1]$, and use the linguistic terms defined in Table 2. The normalized output q_p determines the direction and relative intensity of the proportional-gain correction, q_i determines those of the integral-gain correction, and q_d determines those of the derivative-gain correction. The symmetric normalized output universes enable bidirectional gain adjustment under under-pressure, over-pressure, and rapidly varying error conditions.

The normalized outputs do not directly represent the actual PID gain correction increments. According to Eq. (1), they are transformed by the effective output scaling coefficients S_p, S_i, and S_d into ΔK_p, ΔK_i, and ΔK_d, respectively. The corresponding gain correction intervals are prescribed as $\Delta K_p \in [-1.1,1.1]$, $\Delta K_i \in \left[-2.0\times10^{-2},2.0\times10^{-2}\right]$, $\Delta K_d \in \left[-1.5\times10^{-2},1.5\times10^{-2}\right]$.

The relatively larger proportional-gain correction range improves pressure-error correction during pressure-platform transitions. The smaller integral-gain correction range reduces residual steady-state errors while limiting excessive integral action. The derivative-gain correction range is selected to suppress rapid error variations and pressure overshoot without introducing excessive sensitivity to transient pressure fluctuations. The normalized output membership functions of q_p, q_i, and q_d are shown in Figures 9–11.

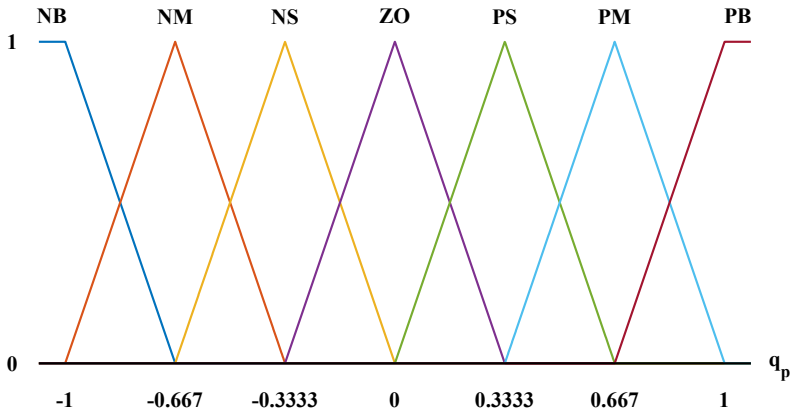


Figure 9. Membership function curves of the normalized fuzzy output q_p

ISSN: 2472-3703 DOI: 10.6911/WSRJ.202611_12(11).0009

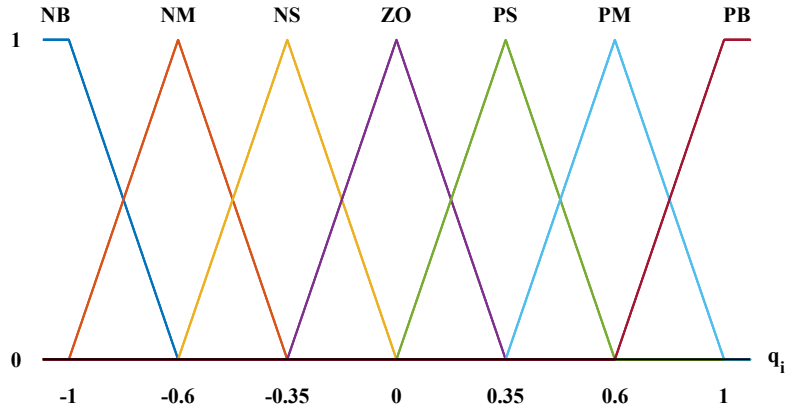


Figure 10. Membership function curves of the normalized fuzzy output q_i

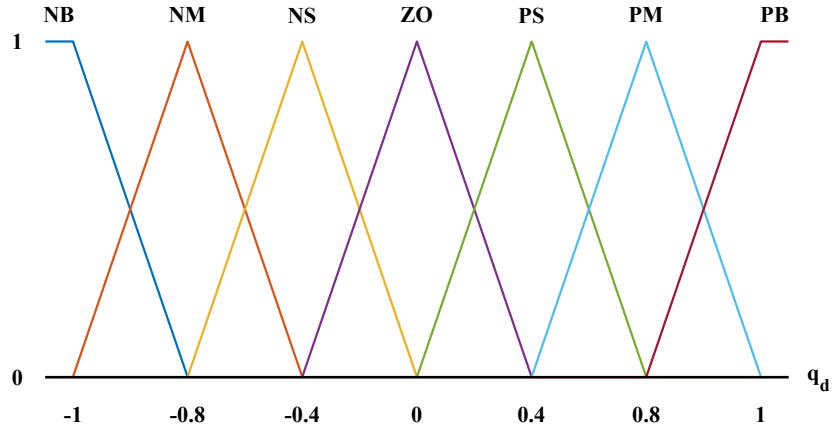


Figure 11. Membership function curves of the normalized fuzzy output q_d

3.2.3 Nonlinear Input Scaling for Variable-Universe Adjustment

Conventional fuzzy PID controllers generally employ fixed input universes, such that large-error and small-error operating conditions are processed using the same inference scale. In the zone-controlled crown roll hydraulic loading system, relatively large pressure errors occur during pressure-platform switching, whereas high local sensitivity is required during steady-state pressure holding and disturbance recovery. Therefore, an input-side nonlinear mapping is introduced to smoothly compress large normalized inputs while preserving the local sensitivity of small inputs.

Let $x \in \mathbb{R}$ denote either of the normalized controller inputs e_N or e_{cN}, and let $\phi(x)$ denote the corresponding input supplied to the fuzzy inference system before the final numerical saturation. Rather than selecting the mapping solely on an empirical basis, it is constructed according to the following requirements: origin preservation and odd symmetry, so that positive and negative errors are treated symmetrically; unit local gain at the origin, so that small errors are not attenuated; strict monotonicity and non-expansiveness, so that the error ordering is preserved without amplifying input perturbations; a finite asymptotic bound compatible with the normalized fuzzy universe; and a single-parameter algebraic form suitable for real-time implementation.

For $x \geq 0$, define the incremental sensitivity of the mapping as $s(x) = \dfrac{d\phi(x)}{dx}$. Consider the one-parameter rational sensitivity family

ISSN: 2472-3703 DOI: 10.6911/WSRJ.202611_12(11).0009

$$s_p(r) = \frac{1}{(1+\alpha r)^p}, \qquad \alpha > 0, \quad p > 0 \tag{3}$$

A bounded mapping requires the total sensitivity over the positive real axis to be finite. For this family,

$$\int_0^{\infty} s_p(r)dr = \frac{1}{\alpha(p-1)}, \qquad p > 1 \tag{4}$$

Therefore, $p > 1$ is required to obtain a finite output bound. The lowest-order integer member satisfying this condition is $p = 2$. Integrating this sensitivity profile from the origin and extending the result by odd symmetry gives

$$\phi(x) = \mathrm{sgn}(x)\int_0^{|x|} \frac{1}{(1+\alpha r)^2}dr = \frac{x}{1+\alpha\,|x|} \tag{5}$$

Accordingly, the associated dynamic scaling factor is

$$\eta(x) = \begin{cases} \dfrac{1}{1+\alpha\,|x|}, & x \neq 0, \\ 1, & x = 0 \end{cases} \tag{6}$$

Where the value at $x = 0$ is defined by continuity.

The pressure error and its rate of change are first mapped to dimensionless normalized variables:

$$e_{\mathrm{N}} = K_e e \tag{7}$$

$$ec_{\mathrm{N}} = K_{ec} ec \tag{8}$$

Where K_e and K_{ec} are the input scaling factors of the pressure error and error rate, respectively. The intermediate fuzzy inputs are then expressed as

$$\tilde{e} = \phi_e\left(e_{\mathrm{N}}\right) = \frac{e_{\mathrm{N}}}{1+\alpha_e\left|e_{\mathrm{N}}\right|} \tag{9}$$

$$\widetilde{ec} = \phi_{ec}(ec_{\mathrm{N}}) = \frac{ec_{\mathrm{N}}}{1+\alpha_{ec}|ec_{\mathrm{N}}|} \tag{10}$$

The final fuzzy inference inputs are given by

$$e^* = \mathrm{sat}\left(\tilde{e}, -1, 1\right) \tag{11}$$

$$ec^* = \mathrm{sat}(\widetilde{ec}, -1, 1) \tag{12}$$

Where $\mathrm{sat}(\cdot)$ denotes the saturation function.

ISSN: 2472-3703 DOI: 10.6911/WSRJ.202611_12(11).0009

The resulting mapping has several useful analytical properties. It is odd and continuously differentiable, and its derivative is

$$\phi'(x) = \frac{1}{(1+\alpha|x|)^2}, \quad x \in \mathbb{R} \tag{13}$$

From Eq. (13),

$$0 < \phi'(x) \leq 1 \tag{14}$$

Which indicates that the mapping is strictly increasing and globally non-expansive. By the mean-value theorem,

$$\left|\phi(x_1) - \phi(x_2)\right| \leq \left|x_1 - x_2\right| \tag{15}$$

So the nonlinear input transformation itself does not amplify small measurement perturbations. Near the origin,

$$\phi(x) = x - \alpha x \,|\, x \,| + O\left(|\, x \,|^3\right), \qquad |\, x \,| \to 0 \tag{16}$$

And hence $\phi'(0) = 1$, showing that the original small-error sensitivity is retained. For large inputs,

$$\lim_{x \to \pm\infty} \phi(x) = \pm \frac{1}{\alpha} \tag{17}$$

And therefore

$$|\, \phi(x) \,| < \frac{1}{\alpha} \tag{18}$$

Consequently, the mapping provides an approximately linear response near the origin and a smooth algebraic compression as the normalized input magnitude increases.

In the present controller, $\alpha_e = \alpha_{ec} = 1$. Accordingly, the asymptotic range of each nonlinear mapping is $(-1,1)$, consistent with the normalized input universe of the fuzzy inference system. The input scaling factors K_e and K_{ec} are retained as optimization variables to align the physical error ranges with the effective transition regions of the mappings. Under this setting, $|\tilde{e}| < 1$ and $|\widetilde{ec}| < 1$ are theoretically guaranteed, while the subsequent saturation blocks serve only as numerical safeguards for finite-precision implementation.

Overall, the rational mapping is monotonic and non-expansive, with algebraically decaying sensitivity as the input magnitude increases. This behavior preserves input discrimination in the small- and moderate-error regions while smoothly compressing large normalized inputs toward the fuzzy-universe boundaries.

3.2.4 Gain Projection, Actuator Saturation, and Tracking Anti-Windup

To distinguish the boundedness of the fuzzy correction signals from that of the gains actually supplied to the controller, the normalized fuzzy outputs q_{p}, q_{i}, and q_{d} were directly monitored at the output of the fuzzy inference block in the subsequent numerical verification. Their prescribed interval was $[-1,1]$. After output scaling, the corresponding gain correction increments were constrained to $\Delta K_{\mathrm{p}} \in [-1.1,1.1]$, $\Delta K_{\mathrm{i}} \in [-0.02,0.02]$, and

ISSN: 2472-3703 DOI: 10.6911/WSRJ.202611_12(11).0009

$\Delta K_{\mathrm{d}} \in [-0.015, 0.015]$. Therefore, the boundedness verification in Section 4.8 separately reports the observed intervals of the normalized fuzzy outputs and the gain correction increments.

Because the fuzzy correction increments may temporarily produce infeasible preliminary gains during pressure-platform switching, an explicit bounded projection is applied. The saturation operator is defined as:

$$\mathrm{sat}(x; x_{\min}, x_{\max}) = \min\left\{x_{\max}, \max\left(x_{\min}, x\right)\right\} \tag{19}$$

The gains actually supplied to the PID controller are then calculated as:

$$\begin{cases} K_{\mathrm{p}}(t) = \mathrm{sat}\left(K_{\mathrm{p,pre}}(t); 0.10, 0.95\right) \\ K_{\mathrm{i}}(t) = \mathrm{sat}\left(K_{\mathrm{i,pre}}(t); 0, 0.04\right) \\ K_{\mathrm{d}}(t) = \mathrm{sat}\left(K_{\mathrm{d,pre}}(t); 0, 0.032\right) \end{cases} \tag{20}$$

These projection intervals were selected on the basis of preliminary closed-loop tuning, the admissible gain ranges of the implemented controller, and repeated co-simulation tests. The projection operation does not alter the fuzzy inference rules; it only prevents the online correction from generating inadmissible gains.

The unconstrained PID command consists of the proportional, integral, and derivative contributions and is expressed as

$$u_{\mathrm{raw}}(t) = u_{\mathrm{P}}(t) + x_{\mathrm{I}}(t) + u_{\mathrm{D}}(t) \tag{21}$$

Here, u_{P}, x_{I}, and u_{D} denote the proportional, integral, and derivative contributions to the unconstrained PID command, respectively. To satisfy the physical input range of the electro-hydraulic proportional pressure-reducing valve, the saturation operator defined in Eq. (19) is applied to obtain the realizable actuator command:

$$u_{\mathrm{sat}}(t) = \mathrm{sat}\left(u_{\mathrm{raw}}(t); 0, 40\right)\ \mathrm{mA} \tag{22}$$

The current delivered to the AMESim plant is denoted by u_{applied}. Because the equivalent disturbance is introduced through a separate plant-side disturbance channel rather than being directly superimposed on the valve-control current, the physical actuator command satisfies

$$u_{\mathrm{applied}}(t) = u_{\mathrm{sat}}(t) \tag{23}$$

A tracking anti-windup structure is employed by returning the realizable command to the tracking port of the PID controller. In the present implementation, the tracking input is defined as

$$u_{\mathrm{trk}}(t) = u_{\mathrm{sat}}(t) \tag{24}$$

To characterize the occurrence, direction, and extent of actuator saturation, the signed saturation residual is defined as

ISSN: 2472-3703 DOI: 10.6911/WSRJ.202611_12(11).0009

$$r_{\text{sat}}(t) = u_{\text{sat}}(t) - u_{\text{raw}}(t) \tag{25}$$

The tracking mismatch acting on the anti-windup path is defined as the difference between the tracking input and the unconstrained PID command. According to Eqs. (24) and (25), it can be written as

$$e_{\text{aw}}(t) = u_{\text{trk}}(t) - u_{\text{raw}}(t) = u_{\text{sat}}(t) - u_{\text{raw}}(t) = r_{\text{sat}}(t) \tag{26}$$

When the unconstrained PID command remains within the physical actuator range, the saturation residual and tracking mismatch are both zero. Once either actuator limit becomes active, the saturation residual becomes nonzero, and the corresponding tracking mismatch feeds the difference between the realizable and unconstrained commands back to the PID controller. This feedback adjusts the internal controller state toward a value compatible with the realizable actuator command, thereby suppressing continued integral accumulation during saturation and facilitating recovery after the actuator constraint is released.

It should be emphasized that x_{I} is an internal integral contribution to the unconstrained PID command rather than the physical current directly applied to the proportional pressure-reducing valve. Therefore, x_{I} is not individually restricted to the physical actuator range of 0–40 mA. This constraint is imposed on u_{sat} and u_{applied}.

3.3. IFE-WOA Parameter Optimization Algorithm

3.3.1 Standard Whale Optimization Algorithm

The whale optimization algorithm, proposed by Mirjalili and Lewis, is a swarm intelligence optimization algorithm. Its search process mainly includes three stages: encircling prey, bubble-net attacking, and searching for prey [33].

In the encircling prey stage, the current best individual in the population is regarded as the target position, and the remaining individuals update their positions according to this target:

$$D = \left| C \cdot X^{*}(t) - X(t) \right| \tag{27}$$

$$X(t+1) = X^{*}(t) - A \cdot D \tag{28}$$

$X^{*}(\mathrm{t})$ is the current best parameter vector, and $X(t)$ is the candidate vector being updated. The iteration index is t. The vector D describes the scaled distance between the positions, while A and C control the update direction and search range.

$$A = 2a \cdot r_1 - a \tag{29}$$

$$C = 2 \cdot r_2 \tag{30}$$

Here, r_1 and r_2 are random coefficients within [0, 1], and a is a convergence factor that gradually decreases with the number of iterations. As a decreases, the variation range of the coefficient vector A gradually narrows, causing the algorithm to shift from global search to local search.

The bubble-net attacking stage includes two modes, shrinking encircling and spiral updating. The position update equation is expressed as:

ISSN: 2472-3703 DOI: 10.6911/WSRJ.202611_12(11).0009

$$X(t+1)=\begin{cases}X^{*}(t)-A\cdot D, & p<0.5\\ D^{'}\cdot \mathrm{e}^{bl}\cdot\cos(2\pi l)+X^{*}(t), & p\geq 0.5\end{cases} \tag{31}$$

Where p determines the selected update mode. The distance term $D^{'}=\left|X^{*}(t)-X(t)\right|$ is determined by the current candidate individual and the best individual; b controls the spiral curvature, and l is sampled within [−1, 1].

In the prey-searching stage, when $\left|A\right|\geq 1$, the whale individual no longer updates its position with respect to the current best solution. Instead, it randomly selects another individual from the population as the reference position:

$$X(t+1)=X_{\mathrm{rand}}(t)-A\cdot D_{\mathrm{rand}} \tag{32}$$

$$D_{\mathrm{rand}}=\left|C\cdot X_{\mathrm{rand}}(t)-X(t)\right| \tag{33}$$

$X_{\mathrm{rand}}(t)$ is a randomly sampled reference individual used for global exploration.

To address the tendency of the standard WOA to suffer from population aggregation, reduced search diversity, and premature convergence in later iterations, existing studies have improved the convergence speed, search accuracy, and stability of the algorithm by introducing inertia weights and dynamic parameter adjustment strategies [34]. On this basis, and considering the control requirements of multi-pressure-platform tracking and local disturbance suppression in the zone-controlled crown roll hydraulic loading system, this paper constructs an IFE-WOA-based optimization strategy for parameter tuning of the variable-universe fuzzy PID controller.

3.3.2 Joint Optimization variables and parameter bounds

The control performance of the variable-universe fuzzy PID controller depends not only on the fuzzy rules, but also on the coordinated selection of the initial PID gains and the input/output scaling factors. Therefore, $X=\left[K_{\mathrm{p0}},K_{\mathrm{i0}},K_{\mathrm{d0}},K_{e},K_{ec},K_{u}\right]$ is selected as the optimization variable vector. Here, K_{p0}, K_{i0}, and K_{d0} denote the initial PID gains; K_{e} and K_{ec} map the pressure error and its rate of change to the fuzzy input range, respectively; and K_{u} is the optimized common output-scaling factor. The lower bounds of the optimization variables are set to [0.2000, 0.0000, 0.0010, 0.0100, 0.0005, 0.0200], and the upper bounds are set to [0.5000, 0.0800, 0.0500, 0.1200, 0.0400, 0.3500]. These parameter bounds are determined based on the control input range of the proportional pressure-reducing valve, conventional PID pre-tuning results, and multiple stability simulation tests. They ensure that candidate parameters have sufficient search space while maintaining stable system responses.

3.3.3 Multi-condition comprehensive fitness function

Considering that the investigated system involves multi-pressure-platform switching and input-side equivalent disturbances, the comprehensive fitness function is defined as:

$$J=J_{\mathrm{nom}}+\lambda J_{\mathrm{dis}} \tag{34}$$

J consists of the nominal tracking term J_{nom} and the disturbance-condition term J_{dis}. The weighting coefficient λ is set to 0.92 as an engineering compromise between nominal tracking and disturbance rejection; the resulting contribution balance and the local sensitivity of this setting are further examined in Section 4.5. To eliminate the influence of different pressure step

ISSN: 2472-3703 DOI: 10.6911/WSRJ.202611_12(11).0009

amplitudes among pressure platforms on the evaluation results, the pressure error in each stage is normalized by the corresponding step amplitude.

The nominal-condition fitness function can be expressed as:

$$J_{\text{nom}} = \sum_{k=1}^{4} \left(w_1 \text{IAE}_k + w_2 \text{ITAE}_k + w_3 M_{\text{p},k} + w_4 e_{\text{ss},k} + w_5 R_k \right) \tag{35}$$

IAE_k and ITAE_k measure the accumulated normalized error and the time-weighted normalized error of the k-th pressure plateau, respectively. $M_{\text{p},k}$ gives the maximum relative overshoot, $e_{\text{ss},k}$ is the average relative steady-state error, and R_k describes the pressure fluctuation during steady holding. The coefficients w_1 - w_5 are used to balance these tracking indices.

The disturbance-condition fitness can be expressed as follows:

$$J_{\text{dis}} = w_6 e_{\text{p},7} + w_7 \text{IAE}_7 + w_8 e_{\text{rec},7} + w_9 e_{\text{p},15} + w_{10} \text{IAE}_{15} \tag{36}$$

Where $e_{\text{p},7}$ and $e_{\text{p},15}$ are the peak absolute errors in the 7 s positive disturbance window and the 15 s negative disturbance window, respectively. IAE_7 and IAE_{15} represent the accumulated absolute errors in the two windows, and $e_{\text{rec},7}$ evaluates the residual error after the 7 s disturbance is removed.

3.3.4 Population-state evaluation based on intuitionistic fuzzy entropy

To evaluate the population aggregation state, the i-th individual X_i^t in the t-th generation and the current best individual X_{best}^t are normalized to obtain Z_i^t and Z_{best}^t, respectively. The relative distance d_i of each individual is then calculated as follows:

$$d_i = \frac{\left| Z_i^t - Z_{\text{best}}^t \right|}{\max\left(\left\| Z^t - Z_{\text{best}}^t \right\|_2 \right) + \varepsilon} \tag{37}$$

Here, ε is a sufficiently small positive constant. Subsequently, the membership degree μ_i, non-membership degree ν_i, and hesitation degree π_i of the intuitionistic fuzzy set are constructed from the relative distance d_i as follows:

$$\mu_i = \max(0, 1 - d_i) \tag{38}$$

$$\nu_i = \begin{cases} 0, & d_i \le 0.5 \\ 2(d_i - 0.5), & d_i > 0.5 \end{cases} \tag{39}$$

$$\pi_i = 1 - \mu_i - \nu_i \tag{40}$$

The value of μ_i increases as an individual approaches the current best solution, whereas ν_i increases when the individual moves away from it. The hesitation degree π_i reflects the uncertainty of the individual distribution.

ISSN: 2472-3703 DOI: 10.6911/WSRJ.202611_12(11).0009

The individual intuitionistic fuzzy entropy and the population-averaged entropy are defined as follows:

$$e_i = \pi_i + \left((1-\pi_i)\left(1-\left|\mu_i - \nu_i\right|\right)\right) \tag{41}$$

$$E^t = \frac{1}{N}\sum_{i=1}^{N} e_i \tag{42}$$

A larger E^t indicates a more dispersed population, whereas a smaller E^t indicates that individuals are concentrated near the current best solution and that the search may have entered local stagnation.

3.3.5 Entropy-driven escape mechanism and position update

To smooth the variation in search step size, this paper uses a nonlinear convergence factor and inertia weight to guide the position update process:

$$a = 2\left[1-\left(\frac{t}{\mathrm{MaxIt}}\right)^{\gamma_a}\right] \tag{43}$$

$$w_{\mathrm{time}} = w_{\max} - \left(w_{\max} - w_{\min}\right)\left(\frac{t}{\mathrm{MaxIt}}\right)^{\gamma_w} \tag{44}$$

$$w = w_{\min} + \left(w_{\mathrm{time}} - w_{\min}\right)E^t \tag{45}$$

In this study, the population size is set to $N = 12$, and the maximum number of iterations is set to $\mathrm{MaxIt} = 25$. The inertia weight parameters are set to $w_{\max} = 0.9$ and $w_{\min} = 0.4$, while the time-decreasing adjustment exponents are set to $\gamma_a = 2.0$ and $\gamma_w = 1.0$.

After the candidate position X_{woa} is generated by the standard WOA, the position-migration operation is defined as follows:

$$X_{\mathrm{new}} = X_i + w\left(X_{\mathrm{woa}} - X_i\right) \tag{46}$$

X_{i} is the current parameter vector of the i-th individual, X_{woa} is the candidate vector generated by the standard WOA update, and X_{new} is the migrated vector after inertia-weight correction.

The key improvement of IFE-WOA is that intuitionistic fuzzy entropy is directly mapped to the escape probability. Unlike entropy-based inertia-weight adjustment, this mechanism directly controls whether escape search is activated according to the population aggregation state. A low entropy value indicates population aggregation around the current best solution and increases the risk of local stagnation; therefore, escape search is triggered with a higher probability. In contrast, a high entropy value indicates sufficient population diversity, so the algorithm mainly follows the standard WOA update path. Based on this idea, the intuitionistic fuzzy entropy-driven escape probability is constructed as:

$$P_e(E^t, t) = \max\left(P_{e,\min} + \left(P_{e,\max} - P_{e,\min}\right)\left(1-E^t\right), P_{e,\mathrm{time0}}\left(1-\frac{t}{\mathrm{MaxIt}}\right)\right) \tag{47}$$

ISSN: 2472-3703 DOI: 10.6911/WSRJ.202611_12(11).0009

$P_e(E^t,t)$ is the escape probability at iteration t. $P_{e,\min}$ and $P_{e,\max}$ set its lower and upper limits, and $P_{e,\text{time0}}$ controls the initial level of the time-decaying escape term. In this study, $P_{e,\min}=0.10$, $P_{e,\max}=0.60$ and $P_{e,\text{time0}}=0.25$. This formulation increases the escape probability when population entropy decreases and gradually weakens the escape tendency as the iteration proceeds. When $\text{rand}<P_e(E^t,t)$, the Gaussian-perturbation escape update is triggered:

$$X_{\text{new}}=X_{\text{best}}+\sigma\cdot\text{randn}(1,D) \tag{48}$$

$$\sigma=0.10\left(U_b-L_b\right)\left(1-\frac{t}{\text{MaxIt}}\right) \tag{49}$$

X_{best} is the best parameter vector found so far, and $\text{randn}(1,D)$ is a D-dimensional standard normal random vector. The search bounds are given by U_b and L_b, while σ controls the amplitude of the Gaussian perturbation. This mechanism expands the search range in the early iterations and performs local refinement around promising parameter combinations in the later iterations.

Unlike WOA variants in which diversity enhancement is governed mainly by a prescribed iteration schedule, the proposed mechanism uses the population entropy E^t as state feedback. According to Eq. (47), the escape probability is a non-increasing function of E^t. Therefore, when the population contracts around the current best solution and the entropy decreases, the probability of activating the escape operator increases. When sufficient diversity is retained, the standard WOA update is preserved, avoiding unnecessary perturbation of the exploitation process. Moreover, the Gaussian perturbation centered on the current best solution has a nonzero probability of crossing its local attraction basin, while the decreasing perturbation amplitude provides a gradual transition from broad exploration to local refinement. Consequently, the proposed mechanism is expected to reduce premature-convergence risk more selectively than schedule-only parameter adjustment, without continuously disrupting exploitation. This state-dependent advantage does not imply universal superiority over every WOA variant, because the relative performance remains problem dependent.

3.3.6 Convergence and Computational Complexity

Let $\Omega=\left[\mathbf{L},\mathbf{U}\right]$ denote the bounded search domain, and assume that the fitness function $f:\Omega\to\mathbb{R}$ is continuous and bounded from below. All updated candidates are projected onto Ω, and the best-so-far solution is retained during the iterative process. Let $f_{\text{best}}^{(t)}$ denote the best fitness value obtained up to iteration t. The elitist retention strategy gives

$$f^\star\le f_{\text{best}}^{(t+1)}\le f_{\text{best}}^{(t)},\qquad \lim_{t\to\infty}f_{\text{best}}^{(t)}=\bar{f}\ge f^\star \tag{50}$$

Where $f^\star$ is the global minimum over Ω. Hence, the best-so-far fitness sequence is non-increasing and bounded from below and therefore converges to a finite limit. This establishes convergence of the objective-value sequence, although it does not imply deterministic attainment of the global optimum within a finite stochastic run.

The entropy-driven escape operation further provides a probabilistic mechanism for approaching the global optimum. Let $S_\varepsilon=\{\mathbf{x}\in\Omega:f(\mathbf{x})\le f^\star+\varepsilon\}$ denote an ε-optimal region with positive measure, and let $q_{\varepsilon,t}>0$ be the conditional probability that a Gaussian

ISSN: 2472-3703 DOI: 10.6911/WSRJ.202611_12(11).0009

escape at iteration t enters S_ε. Because $P_e\left(E^t,t\right)\geq P_{e,\min}>0$, the probability of visiting S_ε within T iterations satisfies

$$\Pr\left\{\min_{0\leq\tau\leq T} f_{\text{best}}^{(\tau)}\leq f^{\text{å}}+\varepsilon\right\}\geq 1-\prod_{t=0}^{T-1}\left(1-P_{e,\min}q_{\varepsilon,t}\right)^N \tag{51}$$

Therefore, the escape mechanism gives every positive-measure neighborhood of the global optimum a positive probability of being reached within the finite search horizon. If persistent exploration is maintained such that $q_{\varepsilon,t}\geq q_\varepsilon>0$, the lower bound approaches one as the evaluation budget increases. This result should be interpreted as a conditional probabilistic convergence property rather than a deterministic global-optimality guarantee.

Regarding computational cost, the standard WOA position update requires $\mathcal{O}(ND)$ operations per iteration. Population normalization, distance calculation, intuitionistic fuzzy entropy evaluation, Gaussian perturbation, and boundary handling also require at most $\mathcal{O}(ND)$ operations. If the cost of one fitness evaluation is denoted by C_f the total time and space complexities are

$$\mathcal{C}_{\text{IFE-WOA}}=\mathcal{O}\left(NT\left(D+C_f\right)\right),\quad \mathcal{C}_{\text{overhead}}=\mathcal{O}(NDT),\quad \mathcal{S}_{\text{IFE-WOA}}=\mathcal{O}(ND) \tag{52}$$

Thus, when the fitness-evaluation cost is excluded, the proposed entropy and escape operations do not change the $\mathcal{O}(NDT)$ asymptotic order of standard WOA; they only introduce a limited constant-factor overhead. In the present co-simulation-based optimization, the AMESim–MATLAB/Simulink fitness evaluation is the dominant computational cost.

4. SIMULATION RESULTS AND ANALYSIS

4.1. Operating Conditions

After controller design and parameter optimization, an AMESim-MATLAB/Simulink co-simulation model is used to evaluate pressure responses under pressure-platform switching and local disturbance conditions. The Z01 loading sub-zone is selected as the test object, and three controllers are compared: a conventional PID controller, a variable-universe fuzzy PID controller, and the proposed IFE-WOA-optimized variable-universe fuzzy PID controller. For clarity in the figure legends and tables, IFE-WOA in the following figures and tables denotes the IFE-WOA-optimized variable-universe fuzzy PID controller. The comparison is carried out within a PID-based control framework so that the contribution of the proposed gain-adjustment and parameter-optimization strategy can be examined under a unified structure. In this setting, the baseline controllers provide a clear reference for evaluating the improvement brought by the variable-universe fuzzy mechanism and the IFE-WOA tuning process.

The reference-pressure command and equivalent input-disturbance profiles used in the co-simulation are shown in Figure 12. Both the nominal and disturbed conditions employ the same multi-stage reference-pressure sequence,

$$P_{\text{ref}}(t)=\begin{cases}90, & 0\leq t<5\\ 103, & 5\leq t<9\\ 95, & 9\leq t<13\\ 110, & 13\leq t\leq 20\end{cases}\quad \text{bar} \tag{53}$$

Under the nominal condition, the equivalent input disturbance is maintained at zero throughout the simulation:

ISSN: 2472-3703 DOI: 10.6911/WSRJ.202611_12(11).0009

$$d_{\text{nom}}(t) = 0 \tag{54}$$

Under the disturbed condition, a positive rectangular pulse with an amplitude of +2.0 is applied from 7.0 to 7.5 s, followed by a negative pulse with an amplitude of −2.5 from 15.0 to 15.7 s:

$$d_{\text{dist}}(t) = \begin{cases} 2.0, & 7.0 \le t < 7.5 \\ -2.5, & 15.0 \le t < 15.7 \\ 0, & \text{otherwise} \end{cases} \tag{55}$$

The disturbance signal is dimensionless and is introduced through a separate plant-side disturbance channel to represent the equivalent influence of adjacent-zone coupling or load variation. Consequently, the nominal and disturbed cases have identical reference-pressure switching sequences, and their difference lies only in the additional disturbance input.

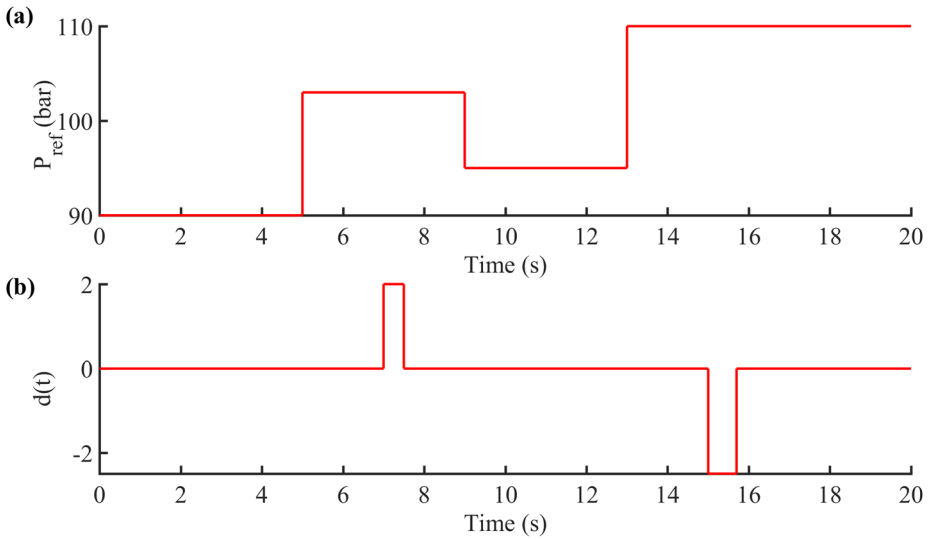


Figure 12. Operating-condition profiles used in the co-simulation: (a) multi-stage reference-pressure command; and (b) dimensionless equivalent disturbance applied through the plant-side disturbance channel under the disturbed condition

4.2. Multi-stage Pressure Step Tracking Performance

As shown in Figure 13, the conventional PID controller exhibits an obvious response lag after reference pressure switching and shows relatively large steady-state deviations during the 95 bar and 110 bar pressure-platform stages. The variable-universe fuzzy PID controller improves the step response characteristics, but local error fluctuations remain. In contrast, the IFE-WOA-optimized variable-universe fuzzy PID controller exhibits more stable tracking performance at all pressure platforms and achieves smaller steady-state tracking errors, especially during the 9-13 s and 13-20 s stages.

ISSN: 2472-3703 DOI: 10.6911/WSRJ.202611_12(11).0009

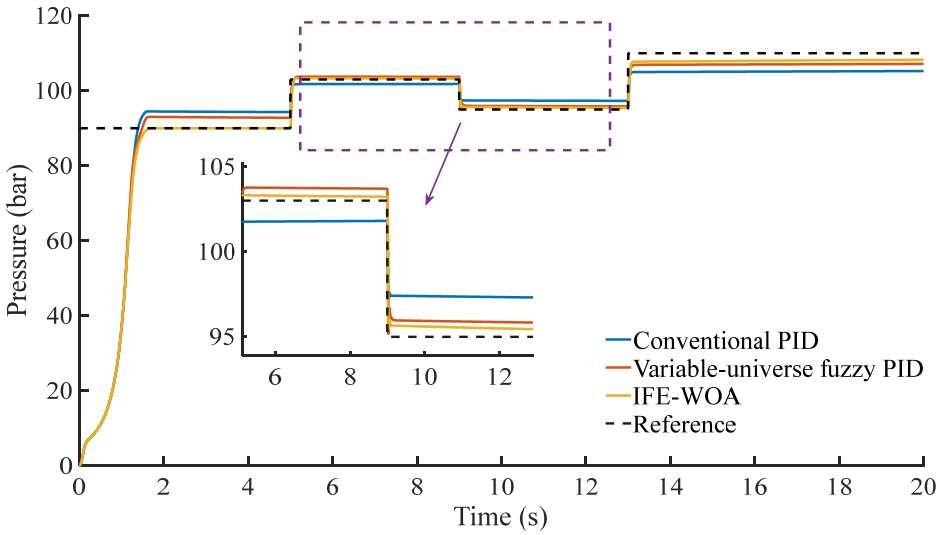


Figure 13. Pressure tracking comparison curves

The error curves in Figure 14 reveal transient increases at each reference pressure switching instant, reflecting the finite dynamic response characteristics of the valve- controlled cylinder system and compressed hydraulic oil. The conventional PID controller shows slower error attenuation and relatively obvious residual errors during the 95 bar and 110 bar pressure-platform stages. The variable-universe fuzzy PID controller reduces the overall error magnitude, but local error peaks still exist after platform switching. In contrast, the IFE-WOA-optimized variable-universe fuzzy PID controller has a faster error attenuation rate and lower steady-state error after pressure switching, indicating better error suppression capability during both platform switching and steady pressure holding.

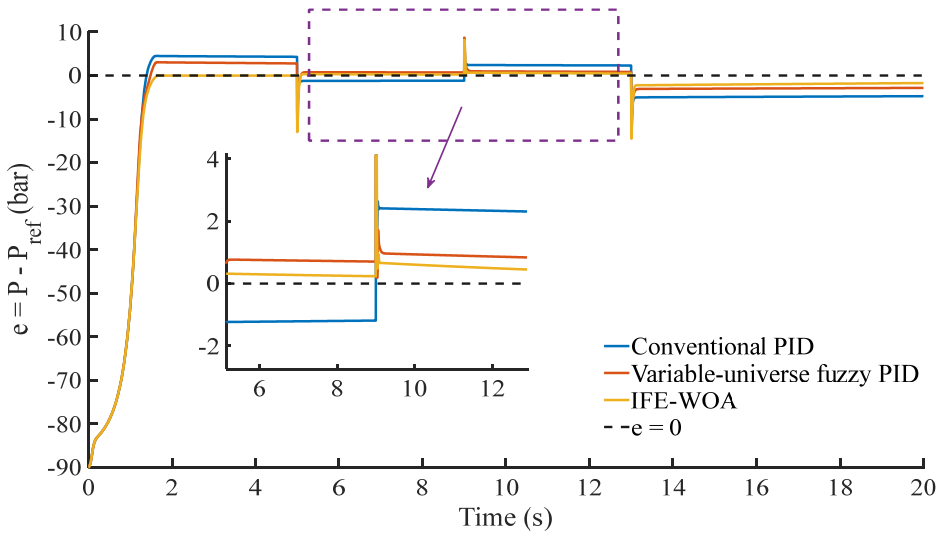


Figure 14. Pressure tracking error comparison curves

4.3. Analysis of Nominal Working Condition Indicators

Table 3 summarizes the nominal-condition performance indices. The IFE-WOA-optimized variable-universe fuzzy PID controller achieves the best overall performance among the three methods. Specifically, the normalized integral of time-weighted absolute error is reduced to

ISSN: 2472-3703 DOI: 10.6911/WSRJ.202611_12(11).0009

4.2972, the maximum relative overshoot is reduced to 0.0243, and the average relative steady-state error is reduced to 0.0487. These results indicate that the proposed controller can effectively reduce cumulative error, transient overshoot, and steady-state deviation during multi-pressure-platform tracking.

Table 3. Summary performance indices under nominal conditions

Control method	Performance index			
	Normalized IAE (s)	Normalized ITAE (s^2)	Maximum relative overshoot	Average relative steady-state error
Conventional PID	1.8411	12.0460	0.0499	0.1869
Variable-universe fuzzy PID	1.4488	6.9755	0.0590	0.0957
IFE-WOA	1.3112	4.2972	0.0243	0.0487
Reduction of IFE-WOA relative to conventional PID (%)	28.78	64.33	51.30	73.94
Reduction of IFE-WOA relative to variable-universe fuzzy PID (%)	9.50	38.40	58.81	49.11

The error-related indicators in the table are normalized by the corresponding step amplitudes. The normalized absolute error of the k-th pressure stage is defined as $\bar{e}_k(t) = \frac{|P(t) - P_{\mathrm{ref},k}|}{A_k}$, where $A_k = |P_{\mathrm{ref},\ k} - P_{\mathrm{ref},\ k\text{-}1}|$, and $P_{\mathrm{ref},0} = 0$ bar is used for the initial pressure build-up stage. For each step phase, t_0 and t_1 are the start and end times of the phase, respectively, and τ is the elapsed time from t_0. The early response window is defined as $\tau \le \min\left[1.2\mathrm{s}, 0.35(t_1 - t_0)\right]$. The maximum relative overshoot is defined as the maximum positive overshoot in each stage divided by the corresponding step amplitude. The average relative steady-state error is obtained by normalizing the average pressure error over the last 20% of samples in each stage.

4.4. Disturbance Conditions and Local-Window Disturbance Rejection

To evaluate local disturbance rejection capability, the 7 s positive disturbance window and the 15 s negative disturbance window are selected for pressure absolute error analysis, and the results are shown in Figures 15 and 16. In the 7 s positive disturbance window, the peak absolute error of the conventional PID controller is 3.2377 bar, which decreases to 2.3282 bar for the variable-universe fuzzy PID controller and further decreases to 1.9263 bar for the IFE-WOA-optimized variable-universe fuzzy PID controller. In addition, the recovery error after disturbance removal is the smallest for the proposed controller. In the 15 s negative disturbance window, all three controllers exhibit different degrees of negative tracking error, but the IFE-WOA-optimized variable-universe fuzzy PID controller maintains the lowest error level throughout the window, with a peak absolute error of 2.0781 bar. This indicates that the proposed controller achieves lower pressure tracking error in the negative disturbance window.

ISSN: 2472-3703 DOI: 10.6911/WSRJ.202611_12(11).0009

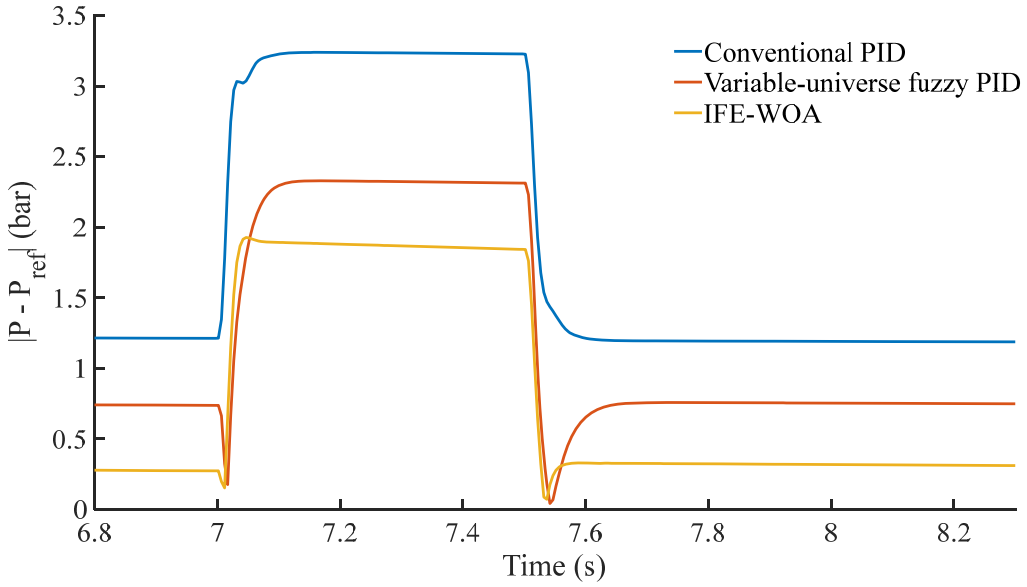


Figure 15. Pressure absolute-error response curves in the 7 s disturbance window

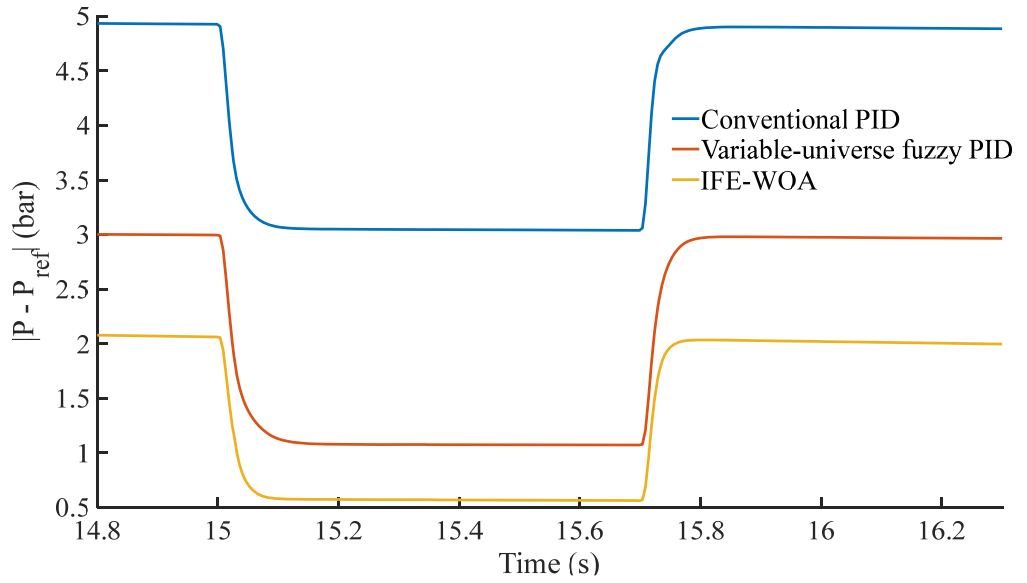


Figure 16. Pressure absolute-error response curves in the 15 s disturbance window

The disturbance-window indices in Table 4 further confirm that the IFE-WOA-optimized variable-universe fuzzy PID controller achieves the lowest peak absolute error and absolute error integral in both disturbance windows. In the 7 s positive disturbance window, the peak absolute error is reduced to 1.9263 bar, and the absolute error integral is reduced to 1.2308 bar·s. In the 15 s negative disturbance window, the peak absolute error is reduced to 2.0781 bar, and the absolute error integral is reduced to 2.0209 bar·s. These results demonstrate that the proposed controller can effectively suppress the transient error increase caused by positive and negative equivalent disturbances and reduce the accumulated error within the disturbance windows, thereby improving local disturbance rejection capability.

ISSN: 2472-3703 DOI: 10.6911/WSRJ.202611_12(11).0009

Table 4. Summary indicators of disturbance rejection in disturbance windows

Control method	7 s positive disturbance window		15 s negative disturbance window	
	Peak absolute error (bar)	IAE under positive disturbance (bar·s)	Peak absolute error (bar)	IAE under negative disturbance (bar·s)
Conventional PID	3.2377	2.8136	4.9351	6.0401
Variable-universe fuzzy PID	2.3282	1.8290	3.0030	3.1313
IFE-WOA	1.9263	1.2308	2.0781	2.0209
Reduction of IFE-WOA relative to conventional PID (%)	40.50	56.26	57.89	66.54
Reduction of IFE-WOA relative to variable-universe fuzzy PID (%)	17.26	32.71	30.80	35.46

The peak absolute error is defined as the maximum value of $\left|P_{\text{ref}}(t)-P(t)\right|$ within the disturbance window, and the integral of absolute error is defined as the integral of the absolute pressure error over the disturbance window. For the 7 s positive disturbance, the analysis window is set to 7.02-8.20 s, where 7.02-7.50 s is defined as the disturbance-holding segment, 7.50-7.55 s as the transition interval after disturbance removal, and 7.55-8.20 s as the post-disturbance recovery segment. For the 15 s negative disturbance, the analysis window is set to 14.95-16.20 s.

4.5. Local Sensitivity Analysis of the Fitness-Function Weighting Coefficient

In the comprehensive fitness function defined in Section 3.3.3, the weighting coefficient λ determines the relative contribution of the disturbed-condition term to the overall optimization criterion. For a fixed controller parameter vector, the direct sensitivity of the comprehensive objective to λ follows from

$$\frac{\partial J}{\partial \lambda}=J_{\text{dis}} \tag{56}$$

Thus, varying λ directly rescales the disturbed-condition contribution, while its practical sensitivity depends on whether moderate variations alter the selected controller solution.

A local sensitivity analysis was performed around the adopted value $\lambda=0.920$ by varying the weighting coefficient by ±20%, resulting in λ=0.736, 0.828, 0.920, 1.012 and 1.104. For each value, the same local candidate set around the optimized IFE-WOA solution was evaluated under identical nominal and disturbed operating profiles.

As shown in Table 5, no parameter switching is observed as λ varies from 0.736 to 1.104, with all five weighting coefficients selecting the same controller parameter set. The variation in the objective value therefore results from reweighting the disturbed-condition contribution rather than from a change in the underlying controller solution. This indicates local robustness of the selected solution to moderate variations in λ, and the adopted value $\lambda=0.920$ is retained as a balanced choice between nominal pressure tracking and disturbance rejection.

ISSN: 2472-3703 DOI: 10.6911/WSRJ.202611_12(11).0009

Table 5. Local sensitivity of the selected controller solution to the weighting coefficient λ

λ	Best objective value	Variation relative to $\lambda = 0.920$ (%)	Selected controller solution
0.736	562.03	-11.87	Same
0.828	599.87	-5.93	Same
0.920	637.71	0.00	Reference
1.012	675.55	+5.93	Same
1.104	713.39	+11.87	Same

4.6. Ablation Study of the IFE-WOA Enhancement Mechanisms

To further identify the individual contributions of the enhancement mechanisms introduced into IFE-WOA, an ablation study was conducted by progressively removing the intuitionistic fuzzy entropy-based population-state evaluation and the escape mechanism. Four optimization variants were considered: standard WOA, IFE-WOA without the escape mechanism, WOA with the escape mechanism but without the entropy-based enhancement, and the complete IFE-WOA. All variants were evaluated using the same parameter bounds and the same multi-condition comprehensive fitness function defined in Section 3.3.3, so that the influence of the algorithmic mechanisms could be examined under a consistent controller-optimization framework.

As shown in Table 6, the complete IFE-WOA achieves the lowest objective value of 637.71, corresponding to a 34.80% reduction relative to standard WOA, whereas the two partially enhanced variants obtain intermediate results. These results indicate complementary contributions of the entropy-based population-state evaluation and escape mechanism in the present engineering ablation screening. The stochastic optimization performance of IFE-WOA is examined separately through the repeated-run analysis in Section 4.7.

Table 6. Ablation results of the enhancement mechanisms in IFE-WOA

Method	Best objective value	Improvement relative to standard WOA (%)	Degradation relative to complete IFE-WOA (%)
Standard WOA-VF-PID	978.04	0.00	53.37
IFE-WOA (no escape)-VF-PID	813.46	16.83	27.56
WOA+escape (no entropy)-VF-PID	849.11	13.18	33.15
Complete IFE-WOA-VF-PID	637.71	34.80	0.00

4.7. Statistical Validation of IFE-WOA

To evaluate the stochastic optimization performance of IFE-WOA, six canonical 30-dimensional benchmark functions, namely Sphere, Rosenbrock, Rastrigin, Ackley, Griewank, and Schwefel, were considered. Standard WOA and IFE-WOA used the same population size ($N = 12$) and maximum number of iterations ($\mathrm{MaxIt} = 25$). Within each paired run, the two algorithms shared the same initial population, and 30 paired runs were independently performed for each function. The final objective values were summarized by the mean, standard deviation (SD), and 95% confidence interval (CI). Paired differences were evaluated using the two-sided Wilcoxon signed-rank test, followed by Holm correction across the six comparisons.

ISSN: 2472-3703 DOI: 10.6911/WSRJ.202611_12(11).0009

Table 7. Statistical comparison of IFE-WOA and standard WOA

Function	Standard WOA	IFE-WOA	Wilcoxon p	Holm-adjusted p
Sphere	$1.303\times10^{4} \pm 4.695\times10^{3}$ [1.128×10^{4}, 1.478×10^{4}]	$1.045\times10^{4} \pm 4.066\times10^{3}$ [8.931×10^{3}, 1.197×10^{4}]	0.0218	0.0655
Rosenbrock	$2.735\times10^{7} \pm 1.851\times10^{7}$ [2.044×10^{7}, 3.426×10^{7}]	$9.605\times10^{6} \pm 7.672\times10^{6}$ [6.740×10^{6}, 1.247×10^{7}]	7.51×10^{-5}	4.51×10^{-4}
Rastrigin	290.54 ± 39.52 [275.78, 305.29]	259.75 ± 46.83 [242.26, 277.24]	0.00873	0.0436
Ackley	17.76 ± 1.94 [17.03, 18.49]	16.62 ± 1.68 [15.99, 17.25]	0.0218	0.0655
Griewank	118.28 ± 42.26 [102.50, 134.06]	95.05 ± 36.59 [81.38, 108.71]	0.0218	0.0655
Schwefel	7209.47 ± 758.72 [6926.16, 7492.79]	7855.23 ± 915.64 [7513.32, 8197.13]	0.0148	0.0592

As shown in Table 7, IFE-WOA achieves lower mean final objective values on five of the six benchmark functions. For these functions, the IFE-WOA win rates range from 63.3% to 86.7%, whereas the win rate on Schwefel is 40.0%. After Holm correction for multiple comparisons, the improvements on Rosenbrock and Rastrigin remain statistically significant. In contrast, standard WOA yields a lower mean objective value on Schwefel, although the difference does not remain significant after Holm correction.

Figure 17 provides a distribution-level view of the paired results, where ratios below unity favor IFE-WOA. The distributions show an overall tendency below unity for five benchmark functions, whereas Schwefel exhibits the opposite tendency. These results further indicate that the optimization benefit of IFE-WOA is problem dependent rather than universal.

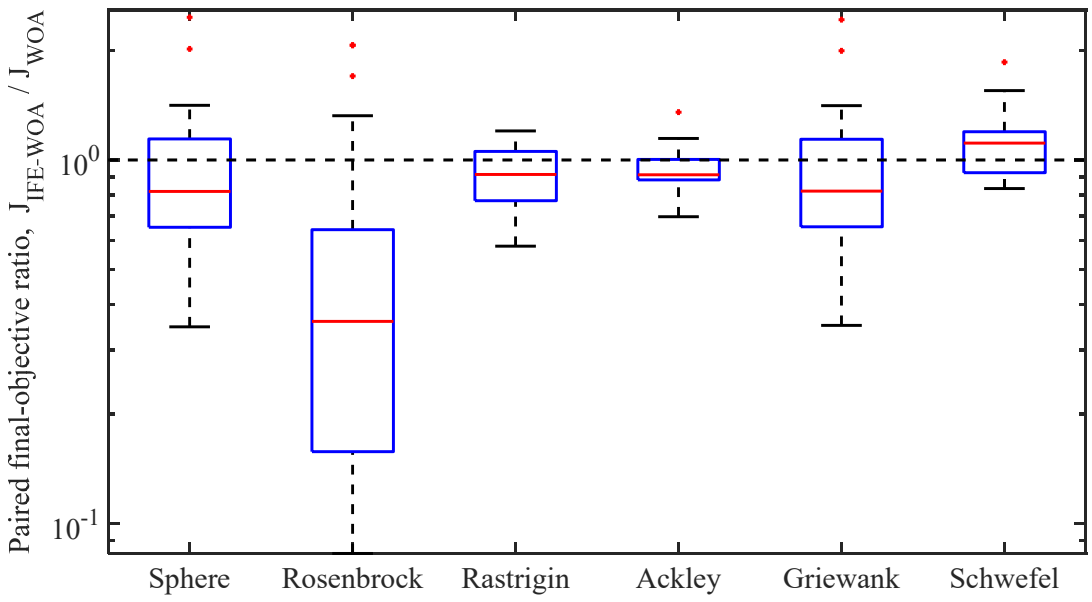


Figure 17. Paired final-objective ratios of IFE-WOA and standard WOA

ISSN: 2472-3703 DOI: 10.6911/WSRJ.202611_12(11).0009

4.8. Verification of Bounded Online Gains and Tracking Anti-Windup

The implementation-level boundedness of the proposed controller was examined under both nominal and disturbed conditions. Because the resulting numerical intervals were identical to the reported precision, Figures 18 and 19 present only the disturbed-condition responses, while Table 8 summarizes the common intervals.

Figure 18 presents the preliminary and projected online PID gains, showing that the preliminary proportional gain temporarily exceeds its prescribed upper boundary during the pressure-platform transition at 9 s, while the projected proportional gain remains limited to 0.95, and that the preliminary integral gain temporarily falls below its admissible lower boundary during pressure switching, whereas the applied integral gain remains non-negative, while the preliminary and projected derivative-gain trajectories completely overlap because the derivative gain remains within its prescribed interval throughout the simulation, thereby confirming that the gain-projection mechanism effectively constrains temporary excursions of the proportional and integral gains, prevents infeasible online gain updates, and avoids unnecessary modifications to gains that already satisfy their constraints.

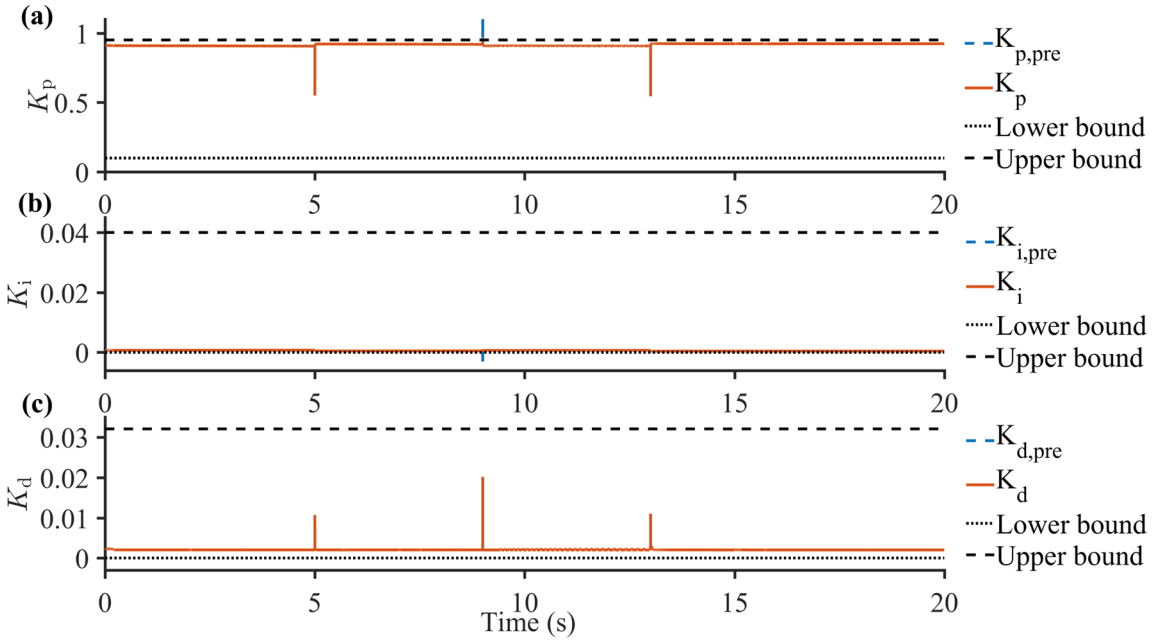


Figure 18. Preliminary and projected online PID gains under the disturbed operating condition: (a) proportional gain; (b) integral gain; and (c) derivative gain

Figure 19(a) shows brief excursions of the unconstrained command beyond the actuator limit, whereas the realizable commands remain within the physical range of 0–40 mA. The saturation residual in Figure 19(b) rapidly returns to zero after each saturation event, while Figure 19(c) shows a bounded integral contribution without persistent accumulation. Although the internal integral contribution x_I can exceed 40 mA, it does not represent the physical actuator current.

ISSN: 2472-3703 DOI: 10.6911/WSRJ.202611_12(11).0009

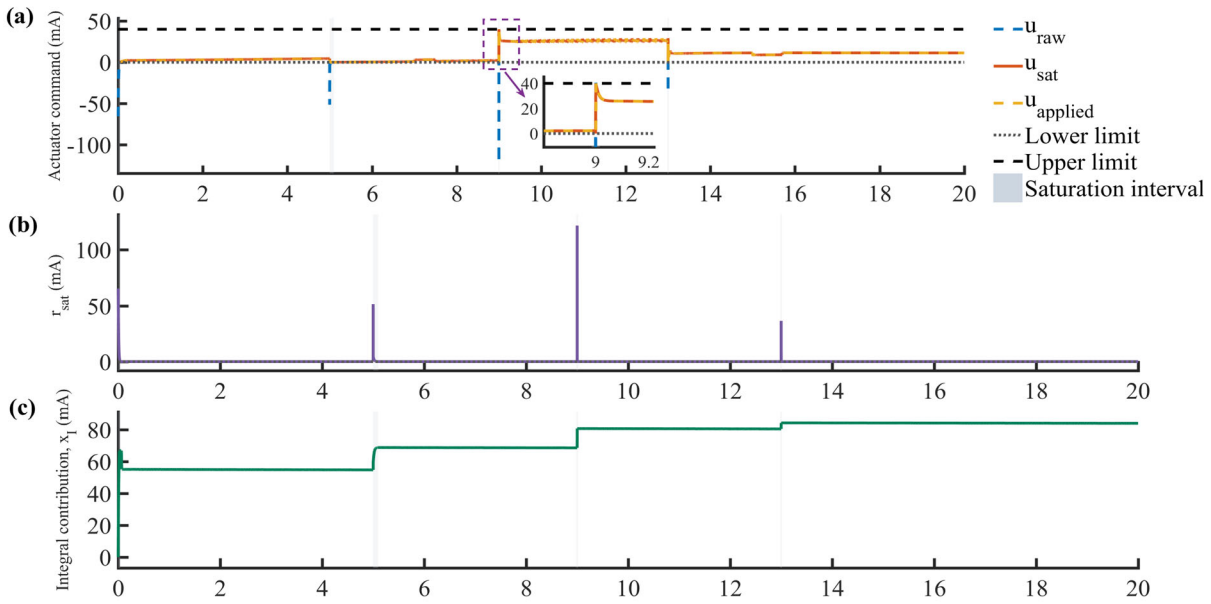


Figure 19. Actuator saturation and tracking anti-windup response under the disturbed operating condition: (a) unconstrained, saturated, and applied actuator commands together with the physical current limits; (b) actuator saturation residual; and (c) internal PID integral contribution

Table 8 confirms that the normalized fuzzy outputs, gain correction increments, projected PID gains, and realizable actuator commands remain within their prescribed intervals under both operating conditions. Boundary contacts indicate activation of the projection mechanism rather than constraint violations.

Table 8. Boundedness verification of the normalized fuzzy outputs, gain correction increments, projected PID gains, and actuator commands under nominal and disturbed operating conditions

Variable	Prescribed interval	Observed interval under both conditions	Result
q_p	$[-1,1]$	$[0.1861,0.7235]$	Pass
q_i	$[-1,1]$	$[-0.7235,-0.5143]$	Pass
q_d	$[-1,1]$	$[-0.3336,0.6749]$	Pass
ΔK_p	$[-1.1,1.1]$	$[0.2047,0.7958]$	Pass
ΔK_i	$[-0.02,0.02]$	$[-0.0147,-0.0103]$	Pass
ΔK_d	$[-0.015,0.015]$	$[-0.0050,0.0101]$	Pass
K_p	$[0.10,0.95]$	$[0.5447,0.9500]$	Pass
K_i	$[0,0.04]$	$[0,0.0007]$	Pass
K_d	$[0,0.032]$	$[0.0020,0.0201]$	Pass
u_{sat}	$[0,40]$ mA	$[0,40]$ mA	Pass
$u_{applied}$	$[0,40]$ mA	$[0,40]$ mA	Pass

ISSN: 2472-3703 DOI: 10.6911/WSRJ.202611_12(11).0009

5. DISCUSSION AND CONCLUSIONS

The proposed framework coordinates constraint-derived variable-universe adjustment, online fuzzy gain correction, and IFE-WOA-based joint tuning under a multi-condition objective. Weighting analysis shows that moderate changes in the disturbance weight do not alter the selected solution, while ablation results demonstrate complementary effects of entropy-based population evaluation and escape. IFE-WOA achieves lower mean objective values on five of six benchmark functions, with significant improvements on Rosenbrock and Rastrigin after Holm correction; the opposite trend on Schwefel indicates problem-dependent benefits. Compared with PID-based baselines, the controller improves pressure tracking, overshoot suppression, steady-state regulation, and disturbance recovery.

Practical application requires further consideration of multi-zone interactions and plant uncertainty. The present single-zone model represents adjacent-zone coupling and load variation through rectangular equivalent disturbances but does not explicitly capture roll-shell deformation, paper-web contact, or coupled hydraulic pressure fields. Variations in fluid properties, leakage, valve nonlinearities, actuator dynamics, and sensor noise may also affect performance. Although bounded mapping, gain projection, actuator saturation, and tracking anti-windup constrain online control actions, the nonlinear time-varying closed loop cannot be fully characterized by one global linear model. Frequency-domain measures obtained through local linearization around quasi-steady operating points would complement the present trajectory-based evaluations. Future work will examine experimentally identified uncertainties, operating-point-dependent frequency characteristics, multi-zone coupling, and hydraulic loading experiments.

In summary, the IFE-WOA-optimized variable-universe fuzzy PID method improves pressure tracking, steady-state holding, and disturbance rejection under the investigated multi-level loading conditions. Its coordinated offline optimization and constrained online adaptation provide a practical PID-based framework for zone-controlled crown roll pressure regulation, subject to further multi-zone and experimental validation.

REFERENCES

[1] Kumar, S., Sharma, S. C., Mahadeva, R., Alawatugoda, J., & Gupta, V. (2023). Robust cross directional controller design for paper machine spatial distributed system. IEEE Access, 11, 53103–53119. https://doi.org/10.1109/ACCESS.2023.3280073.

[2] Kempf, I., Goulart, P. J., & Duncan, S. R. (2024). Control of cross-directional systems with approximate symmetries. Automatica, 167, 111782. https://doi.org/10.1016/j.automatica.2024.111782

[3] Razmjooei, H., Palli, G., Janabi-Sharifi, F., Abdi, E., Terzo, M., & Strano, S. (2023). Adaptive fast-finite-time extended state observer design for uncertain electro-hydraulic systems. European Journal of Control, 69, 100749. https://doi.org/10.1016/j.ejcon.2023.100749

[4] Ba, D. X., Dinh, T. Q., Bae, J., & Ahn, K. K. (2019). An effective disturbance-observer-based nonlinear controller for a pump-controlled hydraulic system. IEEE/ASME Transactions on Mechatronics, 25(1), 32–43. https://doi.org/10.1109/TMECH.2019.2946442

[5] Luo, C., Yao, J., & Gu, J. (2019). Extended-state-observer-based output feedback adaptive control of hydraulic system with continuous friction compensation. Journal of the Franklin Institute, 356(15), 8414–8437. https://doi.org/10.1016/j.jfranklin.2019.08.015

[6] Liu, J., Huang, Y., Helian, B., & Yao, J. (2024). Flow match and precision motion control of asymmetric electro-hydrostatic actuators with complex external force in four-quadrants. Journal of the Franklin Institute, 361(2), 1025–1039. https://doi.org/10.1016/j.jfranklin.2023.11.027

ISSN: 2472-3703 DOI: 10.6911/WSRJ.202611_12(11).0009

[7] Phan, V. D., & Ahn, K. K. (2023). Fault-tolerant control for an electro-hydraulic servo system with sensor fault compensation and disturbance rejection. Nonlinear Dynamics, 111(11), 10131–10146. https://doi.org/10.1007/s11071-023-08364-3

[8] Yang, X., Ge, Y., Deng, W., & Yao, J. (2024). Precision motion control for electro-hydraulic axis systems under unknown time-variant parameters and disturbances. Chinese Journal of Aeronautics, 37(1), 463–471. https://doi.org/10.1016/j.cja.2023.06.001

[9] Li, D., Lu, K., Cheng, Y., & Pan, H. (2024). Nonlinear model predictive control—cross-coupling control with deep neural network feedforward for multi-hydraulic system synchronization control. ISA Transactions, 150, 30–43. https://doi.org/10.1016/j.isatra.2024.05.016

[10] Li, C., Lyu, L., Helian, B., & Yao, J. (2021). Precision motion control of an independent metering hydraulic system with nonlinear flow modeling and compensation. IEEE Transactions on Industrial Electronics, 69(7), 7088–7098. https://doi.org/10.1109/TIE.2021.3097204

[11] Yu, B., Li, H., Ma, G., Liu, X., Chen, C., Zheng, B., Ba, K., & Kong, X. (2024). Design and matching control strategy of electro-hydraulic load-sensitive hydraulic power unit for legged robots. Energy, 313, 133730. https://doi.org/10.1016/j.energy.2024.133730

[12] Helian, B., Mustalahti, P., Mattila, J., & Geimer, M. (2022). Adaptive robust pressure control of variable displacement axial piston pumps with a modified reduced-order dynamic model. Mechatronics, 87, 102879. https://doi.org/10.1016/j.mechatronics.2022.102879

[13] Chen, Z., Helian, B., Zhou, Y., & Geimer, M. (2022). An integrated trajectory planning and motion control strategy of a variable rotational speed pump-controlled electro-hydraulic actuator. IEEE/ASME Transactions on Mechatronics, 28(1), 588–597. https://doi.org/10.1109/TMECH.2022.3209873

[14] Liu, J., Yao, J., & Deng, W. (2024). Nonlinear robust adaptive control of electro-hydrostatic actuators with continuous friction compensation. International Journal of Control, Automation and Systems, 22(4), 1225–1237. https://doi.org/10.1007/s12555-022-1120-6

[15] Hao, X., Xin, Z., Huang, W., Wan, S., Qiu, G., Wang, T., & Wang, Z. (2025). Deep reinforcement learning enhanced PID control for hydraulic servo systems in injection molding machines. Scientific Reports, 15(1), 23005. https://doi.org/10.1038/s41598-025-05904-2

[16] Yao, Z., Xu, F., Jiang, G. P., & Liu, Y. (2023). Data-driven control of hydraulic manipulators by reinforcement learning. IEEE/ASME Transactions on Mechatronics, 29(4), 2673–2684. https://doi.org/10.1109/TMECH.2023.3238928

[17] Yang, Y., Gao, Y., Wu, J., & Wang, Y. (2025). Optimal predictive load frequency control with multi-objective PID-based search algorithm. Swarm and Evolutionary Computation, 99, 102214. https://doi.org/10.1016/j.swevo.2025.102214

[18] Filo, G. (2023). A review of fuzzy logic method development in hydraulic and pneumatic systems. Energies, 16(22), 7584. https://doi.org/10.3390/en16227584

[19] Razmjooei, H., Palli, G., & Abdi, E. (2022). Continuous finite-time extended state observer design for electro-hydraulic systems. Journal of the Franklin Institute, 359(10), 5036–5055. https://doi.org/10.1016/j.jfranklin.2022.04.014

[20] Yang, Y., Gao, Y., Gao, S., & Ding, Z. (2025). Optimising PID controllers for multi-area automatic generation control with improved NSGA-II. CAAI Transactions on Intelligence Technology, 10(4), 1135–1147. https://doi.org/10.1049/cit2.12367

ISSN: 2472-3703 DOI: 10.6911/WSRJ.202611_12(11).0009

[21] Yang, Y., Gao, Y., Ding, Z., & Wu, J. (2024). Advancements in Q-learning meta-heuristic optimization algorithms: A survey. Wiley Interdisciplinary Reviews: Data Mining and Knowledge Discovery, 14(6), e1548. https://doi.org/10.1002/widm.1548

[22] Zhou, Y., & Hao, Z. (2025). Multi-strategy improved whale optimization algorithm and its engineering applications. Biomimetics, 10(1), 47. https://doi.org/10.3390/biomimetics10010047

[23] Shen, Y., Zhang, C., Gharehchopogh, F. S., & Mirjalili, S. (2023). An improved whale optimization algorithm based on multi-population evolution for global optimization and engineering design problems. Expert Systems with Applications, 215, 119269. https://doi.org/10.1016/j.eswa.2022.119269

[24] Chakraborty, S., Saha, A. K., Chakraborty, R., & Mirjalili, S. (2021). An enhanced whale optimization algorithm for large scale optimization problems. Knowledge-Based Systems, 233, 107543. https://doi.org/10.1016/j.knosys.2021.107543

[25] Chakraborty, S., Saha, A. K., Sharma, S., & Mirjalili, S. (2021). A novel enhanced whale optimization algorithm for global optimization. Computers & Industrial Engineering, 153, 107086. https://doi.org/10.1016/j.cie.2020.107086

[26] Li, M., Yu, X., Fu, B., & Li, Y. (2025). A modified whale optimization algorithm with multi-strategy mechanism for global optimization problems. Neural Computing and Applications, 37(27), 22339–22352. https://doi.org/10.1007/s00521-025-10471-2

[27] Yang, Y., Gao, Y., Wu, J., & Ding, Z. (2024). Improving PID controller performance in nonlinear oscillatory automatic generation control systems using a multi-objective marine predator algorithm with enhanced diversity. Journal of Bionic Engineering, 21(5), 2497–2514. https://doi.org/10.1007/s42235-024-00531-0

[28] Rana, N., Latiff, M. S. A., Abdulhamid, S. M., & Ali, M. (2020). Whale optimization algorithm: A systematic review of contemporary applications, modifications and developments. Neural Computing and Applications, 32(20), 16245–16277. https://doi.org/10.1007/s00521-020-04832-1

[29] He, F., Dong, Y., & Hu, B. (2023). Speed control method for the working shaft of the complex hydraulic drive system based on IFE-WOA improved fuzzy PID controller. Applied Artificial Intelligence, 37(1), 2216579. https://doi.org/10.1080/08839514.2023.2216579

[30] Xu, Z., Deng, W., Shen, H., & Yao, J. (2022). Extended-state-observer-based adaptive prescribed performance control for hydraulic systems with full-state constraints. IEEE/ASME Transactions on Mechatronics, 27(6), 5615–5625. https://doi.org/10.1109/TMECH.2022.3149501

[31] Feng, H., Song, Q., Ma, S., & Wen, J. (2022). A new adaptive sliding mode controller based on the RBF neural network for an electro-hydraulic servo system. ISA Transactions, 129, 472–484. https://doi.org/10.1016/j.isatra.2022.08.014

[32] Niu, S., Wang, J., Zhao, J., & Li, Y. (2024). Neural network-based finite-time command-filtered adaptive backstepping control of electro-hydraulic servo system with a three-stage valve. ISA Transactions, 144, 419–435. https://doi.org/10.1016/j.isatra.2024.04.011

[33] Mirjalili, S., & Lewis, A. (2016). The whale optimization algorithm. Advances in Engineering Software, 95, 51–67. https://doi.org/10.1016/j.advengsoft.2016.01.008

[34] Wu, Q. (2025). An enhanced whale optimization algorithm with inertia weight and dynamic parameter adaptation for wireless sensor network deployment. Computing, 107(8), 167. https://doi.org/10.1007/s00607-025-01462-4